

Tracking Volatile Behaviour in Sub-volcanic Plumbing Systems Using Apatite and Glass: Insights into Pre-eruptive Processes at Campi Flegrei, Italy

Michael J. Stock^{1,2*}, Madeleine C. S. Humphreys³, Victoria C. Smith⁴, Roberto Isaia⁵, Richard A. Brooker⁶ and David M. Pyle¹

¹Department of Earth Sciences, University of Oxford, South Parks Road, Oxford OX1 3AN, UK; ²Department of Earth Sciences, University of Cambridge, Downing Street, Cambridge CB2 3EQ, UK; ³Department of Earth Sciences, Durham University, Science Labs, Durham DH1 3LE, UK; ⁴Research Laboratory for Archaeology and the History of Art, University of Oxford, South Parks Road, Oxford OX1 3TG, UK; ⁵Istituto Nazionale di Geofisica e Vulcanologia, Osservatorio Vesuviano, via Diocleziano 328, Napoli 80154, Italy; ⁶School of Earth Sciences, University of Bristol, Queens Road, Bristol BS8 1RJ, UK

*Corresponding author. E-mail: ms2368@cam.ac.uk

Received March 11, 2017; Accepted February 16, 2018

ABSTRACT

Volatile elements play an important role in many aspects of the physicochemical architecture of sub-volcanic plumbing systems, from the liquid line of descent to the dynamics of magma storage and eruption. However, it remains difficult to constrain the behaviour of magmatic volatiles on short timescales before eruption using established petrological techniques (e.g. melt inclusions); specifically, in the final days to months of magma storage. This study presents a detailed model of pre-eruptive volatile behaviour in the Campi Flegrei system (Italy), through combined analyses of apatite crystals and glass. The deposits of eight eruptions were examined, covering the full spectrum of melt compositions, eruptive styles and periods of activity at Campi Flegrei in the past 15 kyr. Measured apatite compositions are compared with thermodynamic models that predict the evolution of the crystal compositions during different fractional crystallization scenarios, including (1) volatile-undersaturated conditions, (2) H₂O-saturated conditions and (3) varying *P*–*T* conditions. The compositions of clinopyroxene-hosted and biotite-hosted apatite inclusions are consistent with crystallization under volatile-undersaturated conditions that persisted until late in magmatic evolution. Apatite microphenocrysts show significantly more compositional diversity, interpreted to reflect a mixed cargo of crystals derived from volatile-undersaturated melts at depth and melts that have undergone cooling and degassing in discrete shallow-crustal magma bodies. Apatite microphenocrysts from lavas show some re-equilibration during cooling at the surface. Clinopyroxene-hosted melt inclusions within the samples typically contain 2–4 wt % H₂O, indicating that they have been reset during temporary magma storage at 1–3 km depth, similar to the depth of sill emplacement during recent seismic crises at Campi Flegrei. Comparable apatite compositional trends are identified in each explosive eruption analysed, regardless of volume, composition or eruption timing. However, apatites from the different epochs of activity appear to indicate subtle changes in the H₂O content of the parental melt feeding the Campi Flegrei system over time. This study demonstrates the potential utility of integrated apatite and glass analysis for investigating pre-eruptive volatile behaviour in apatite-bearing magmas.

Key words: apatite; melt inclusions; Campi Flegrei; volatiles; thermodynamic modelling

INTRODUCTION

Magmatic volatiles (H_2O , CO_2 , halogens and SO_2) are minor but important constituents of most silicate melts, and affect almost every aspect of magmatic evolution and eruption. Volatiles influence mineral phase stability and the liquid line of descent (Grove *et al.*, 2003; Zimmer *et al.*, 2010), as well as melt density (Lange & Carmichael, 1990) and viscosity (Giordano *et al.*, 2008), thus exerting a major control on the depths of magma storage and the crustal-scale structure of sub-volcanic systems (Annen *et al.*, 2006). Volatile exsolution and expansion drives volcanic eruptions, and the pre-eruptive behaviour of volatiles plays an important role in controlling the style and tempo of volcanism at the Earth's surface (Roggensack *et al.*, 1997; Huppert & Woods, 2002; Cashman, 2004; Edmonds, 2008).

Given the fundamental role of volatiles in controlling volcanic processes, quantification of their pre-eruptive concentrations remains a high priority for any investigation. A variety of petrological methods have been used to decipher the volatile histories of past eruptions, giving access to distinct snapshots of melt volatile contents over variable pre-eruptive timescales. For example, melt inclusions capture a record of magmatic volatiles at the time of entrapment, and have been used widely to constrain volatile concentrations in different magmatic settings (e.g. Dunbar *et al.*, 1989; Saal *et al.*, 2002; Wallace, 2005; Stefano *et al.*, 2011). However, recent studies have revealed the rapidity of H^+ diffusion in common igneous phenocrysts under magmatic conditions, relative to the timescales of pre-eruptive magma storage (e.g. Woods *et al.*, 2000; Ingrin & Blanchard, 2006; Reubi *et al.*, 2013). Melt inclusion H_2O contents may diffusively re-equilibrate through their host crystals within hours to weeks, limiting this volatile record to the very final stages of magma storage and/or ascent (e.g. Danyushevsky *et al.*, 2002; Portnyagin *et al.*, 2008; Gaetani *et al.*, 2012; Bucholz *et al.*, 2013; Lloyd *et al.*, 2013; Reubi *et al.*, 2013; Preece *et al.*, 2014). It has also been shown that significant amounts of CO_2 may migrate from the inclusion melt into shrinkage bubbles, leading to underestimates of pressure (Moore *et al.*, 2015). Understanding volatile systematics during late-stage magma storage and the onset of magma ascent is essential for identifying eruption-triggering processes and understanding the 'warning' signs that would be observed at the Earth's surface in the build-up to an eruption.

Apatite [$\text{Ca}_4(\text{PO}_4)_3\text{F}$, Cl, OH] is a common accessory mineral in volcanic, plutonic and ore-forming environments (Piccoli & Candela, 2002) and has received increasing attention as a potential magmatic volatile 'probe', owing to its ability to incorporate all major magmatic volatiles into its crystal structure. Halogens and OH are essential structural constituents in apatite and are incorporated as part of a series of exchange equilibria (Candela, 1986; McCubbin *et al.*, 2015). Sulphate and CO_3^{2-} may also substitute into apatite as

trace components (e.g. Pan & Fleet, 2002; Dietterich & de Silva, 2010; Riker *et al.*, 2018). Recent work has focused on deciphering the relationship between apatite F–Cl–OH compositions and their host melt volatile contents (e.g. Candela, 1986; Piccoli & Candela, 1994; Patiño Douce & Roden, 2006; Boyce & Hervig, 2009; McCubbin *et al.*, 2011; Boyce *et al.*, 2014; Stock *et al.*, 2016). One advantage of apatite analysis is that phenocryst-hosted apatite inclusions can preserve a record of melt volatile compositions under conditions in which melt inclusions may have re-equilibrated (Stock *et al.*, 2016). Because volatile re-equilibration in mineral-hosted apatite inclusions requires simultaneous diffusion of F, Cl and/or OH, this process will be rate-limited by halogen diffusivity in the host phenocrysts, which is significantly slower than that of H^+ (Bucholz *et al.*, 2013; Lloyd *et al.*, 2013). In contrast, F–Cl–OH diffusion within apatite crystals is relatively rapid and microphenocrysts are therefore able to exchange volatiles with their host liquids on geologically short timescales [i.e. microphenocryst rims may re-equilibrate in weeks to years at magmatic temperatures (T); Brenan, 1993]. Because these timescales of apatite microphenocryst re-equilibration are longer than timescales of magma ascent (i.e. hours to days), apatite microphenocrysts may preserve a record of pre-eruptive conditions, even when matrix glasses degas at low pressure [(P); Stock *et al.*, 2016].

In this study, we investigate apatite and glass compositions in juvenile samples from eight eruptions of the Campi Flegrei volcano (Italy), to determine magmatic volatile systematics and processes in the build-up to eruptions. Campi Flegrei was selected as the focus of this study because its melts are known to be apatite-bearing and volatile-rich (D'Antonio *et al.*, 1999; Cannatelli *et al.*, 2007; Arienzo *et al.*, 2010, 2016). It has also recently shown signs of unrest (Chiodini *et al.*, 2012; Moretti *et al.*, 2017). Building on the work of Candela (1986) and Piccoli & Candela (1994) we develop thermodynamic models that predict the theoretical compositional evolution of apatite as a function of changing magma compositions during fractional crystallization in the presence or absence of different fluid phases. Different populations of apatite inclusions (hosted in biotite and clinopyroxene) and microphenocrysts are identified based on their volatile compositions and, through comparison with our thermodynamic models, we use these to constrain the pattern of magmatic volatile behaviour in the sub-volcanic plumbing system at Campi Flegrei. Although melt inclusions have re-equilibrated during magma ascent, coupled interpretation of apatite and glass compositions provides additional constraints on the structure of the Campi Flegrei plumbing system and the composition of the magmatic fluid phase prior to eruption. Finally, we discuss apparent variations in apatite volatile contents that are linked to different periods of eruptive activity at Campi Flegrei, and suggest that the volatile contents of the incoming parental magmas vary with time.

GEOLOGICAL SETTING

Campi Flegrei comprises a nested caldera system, defined by collapse scarps that formed during the Campanian Ignimbrite (~40 ka; [Giaccio *et al.*, 2017](#)) and Neapolitan Yellow Tuff (NYT, ~15 ka; [Deino *et al.*, 2004](#)) eruptions ([Fig. 1](#)). It is one of the most active volcanoes in Europe, having produced >60 eruptions in the past 15 kyr, from vents located within the NYT caldera ([Smith *et al.*, 2011](#)). These are divided into three 'epochs' that represent periods of eruptive activity, separated by prolonged quiescence ([Di Vito *et al.*, 1999](#)). Vents for these eruptions are located within the NYT caldera ([Fig. 1](#); [Di Vito *et al.*, 1999](#); [Isaia *et al.*, 2009](#)). Epoch 1 occurred from ~15 to 10.6 ka and produced ~30 explosive eruptions, with a typical inter-eruptive interval of ~70 years ([Di Vito *et al.*, 1999](#); [Smith *et al.*, 2011](#)). Six low-magnitude explosive eruptions occurred in Epoch 2, between ~9.6 and 9.1 ka, at an average interval of ~65 years ([Di Vito *et al.*, 1999](#); [Smith *et al.*, 2011](#)), followed by a long period (~4 kyr) of quiescence. Twenty-seven eruptions occurred within the short Epoch 3 time-period, between ~5.5 and 3.5 ka ([Smith *et al.*, 2011](#)), with an average eruptive interval of

~75 years ([Di Vito *et al.*, 1999](#)). Most Epoch 3 eruptions were small, explosive events [typically producing 0.02–0.10 km³ of material, dense rock equivalent (DRE); [Smith *et al.*, 2011](#)]. However, uniquely within the past 15 kyr, Epoch 3 also includes four effusive lava domes ([Melluso *et al.*, 1995](#); [Di Vito *et al.*, 1999](#)). The most recent Campi Flegrei eruption was at Monte Nuovo in 1538 CE. This occurred after a >3 kyr dormant period ([Piochi *et al.*, 2005](#)), substantially greater than the typical inter-eruption time interval, and is therefore not considered part of Epoch 3 ([Smith *et al.*, 2011](#)).

Chemical diversity of eruptive products in the past 15 kyr

The most mafic (shoshonitic) melt inclusions identified in Campi Flegrei typify the mantle melts feeding the system ([Mangiacapra *et al.*, 2008](#); [Vetere *et al.*, 2011](#)). Major and trace element studies of Campi Flegrei whole-rocks and glasses show an evolutionary trend from these mafic melts to evolved trachytes or phonolites, with the entire suite formed by fractional crystallization of a single parental magma composition, punctuated by periodic recharge events ([Villemant,](#)

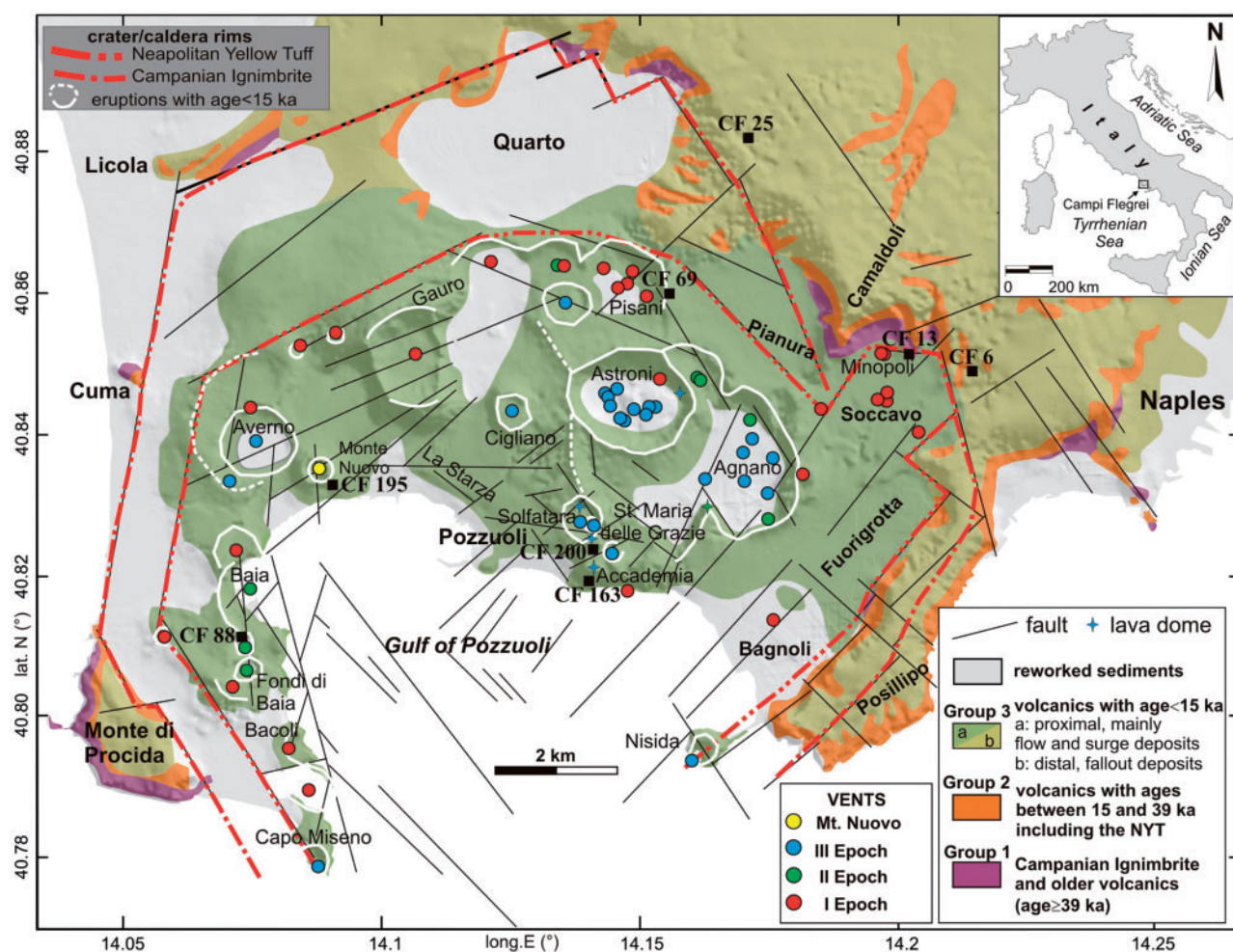


Fig. 1. Simplified geological map of the Campi Flegrei caldera showing major structural features, adapted from [Vitale & Isaia \(2014\)](#). The locations of sampling sites (black squares) and vents for each eruption analysed in this study ([Table 1](#)) are indicated.

1988; Civetta *et al.*, 1991; D'Antonio *et al.*, 1999; Pappalardo *et al.*, 1999; Di Renzo *et al.*, 2011; Di Vito *et al.*, 2011; Smith *et al.*, 2011; Fourmentraux *et al.*, 2012). Pre-NYT (older than 15 ka) melts encompass only the most evolved end of the compositional spectrum (Pappalardo *et al.*, 1999). Post-NYT (younger than 15 ka) magmas do not follow a continual compositional trend between eruptions (i.e. from primitive to evolved), but the most primitive matrix glasses and whole-rocks are derived from Epoch 1, with Epochs 2 and 3 largely indistinguishable based on their major element compositions (D'Antonio *et al.*, 1999; Smith *et al.*, 2011). Matrix glasses from Monte Nuovo are unlike previous eruptions, with notably higher Na₂O concentrations (Smith *et al.*, 2011).

In contrast, isotopic heterogeneity in Campi Flegrei products suggests that the magmas cannot have formed through fractional crystallization alone (Pappalardo *et al.*, 1999, 2002; D'Antonio *et al.*, 2007; Di Renzo *et al.*, 2011). The isotopic compositions of <15 ka Campi Flegrei melts reflect mixing between three distinct end-members, defined by Di Renzo *et al.* (2011) as the 'NYT component' (⁸⁷Sr/⁸⁶Sr 0.70750–0.70753, ¹⁴³Nd/¹⁴⁴Nd ~0.51246, ²⁰⁶Pb/²⁰⁴Pb ~19.04, δ¹¹B ~–7.9‰), the 'Minopoli 2 component' (⁸⁷Sr/⁸⁶Sr ~0.70860, ¹⁴³Nd/¹⁴⁴Nd ~0.51236, ²⁰⁶Pb/²⁰⁴Pb ~18.90, δ¹¹B –7.32‰), and the 'Astroni 6 component' (⁸⁷Sr/⁸⁶Sr ~0.70726, ¹⁴³Nd/¹⁴⁴Nd ~0.51250, ²⁰⁶Pb/²⁰⁴Pb ~19.08, δ¹¹B –9.8‰). The isotopic composition of Campi Flegrei magmas is defined in the deep crust, before significant crystal fractionation, but the major and trace element compositions of these primitive liquids must be closely similar to permit evolution along the same liquid line of descent (Pappalardo *et al.*, 2002). The prevalence of these isotopic components correlates with the different epochs of activity: Epochs 1 and 2 show mixing between 'NYT' and 'Minopoli 2' components; Epoch 3 shows mixing between 'NYT', 'Minopoli 2' and 'Astroni 6' components; the Monte Nuovo eruption sampled near end-member 'Astroni 6 component' melts (Di Renzo *et al.*, 2011). Enriched δ¹¹B in Epochs 1 and 2 reflects a more metasomatized mantle source caused by a higher slab-derived fluid input (D'Antonio *et al.*, 2007) and/or a lower subducted sediment input into the mantle wedge (Tonarini *et al.*, 2004; Di Renzo *et al.*, 2011). Higher ⁸⁷Sr/⁸⁶Sr and lower ¹⁴³Nd/¹⁴⁴Nd and ²⁰⁶Pb/²⁰⁴Pb ratios demonstrate greater crustal assimilation in Epochs 1 and 2 than in Epoch 3 and Monte Nuovo (D'Antonio *et al.*, 2007; Di Renzo *et al.*, 2011). However, the Campi Flegrei liquid line of descent and extent of Sr and Pb isotopic heterogeneity is compatible only with very minor assimilation (D'Antonio *et al.*, 2007; Fowler *et al.*, 2007).

Water contents of Campi Flegrei melt inclusions typically vary from ~1 to ~4 wt % and show no systematic relationship with the degree of magma differentiation (Mangiaccapra *et al.*, 2008; Arienzo *et al.*, 2016; Stock *et al.*, 2016). Campi Flegrei melt inclusions generally have very low CO₂ concentrations (<250 ppm), with a few analyses extending up to 400–500 ppm (Marianelli *et al.*, 2006; Arienzo *et al.*, 2010, 2016; Stock *et al.*, 2016).

SAMPLES AND METHODS

Eruptions studied

The eruptions investigated cover the full range of melt compositions, eruption sizes and styles of activity from Campi Flegrei in the past 15 kyr (Table 1; for full stratigraphy see Smith *et al.*, 2011). Vent locations, average matrix glass compositions and absolute eruption ages for the samples analysed in this study are given in Fig. 1 and Table 1. The Minopoli 1 tuff cone was sampled because it is a small, phono-tephritic to tephri-phonolitic explosive eruption, typical of the early Epoch 1 eruptions that followed the NYT event (Smith *et al.*, 2011). Scoria was also sampled from the slightly larger, slightly more evolved Pisani 1 eruption, which occurred in mid-late Epoch 1 (Smith *et al.*, 2011). Deposits from more recent eruptions are typically more evolved. We sampled Astroni 1 from Epoch 3, which represents the first of seven small explosive eruptions from the Astroni vent between 4 and 4.4 ka (Isaia *et al.*, 2004; Smith *et al.*, 2011). These deposits comprise phreatomagmatic surge beds interbedded with subordinate Strombolian pumice layers (Smith *et al.*, 2011). Pomici Principali (PP) was the largest eruption in the last 15 kyr, generating a Plinian column and pyroclastic density currents (Di Vito *et al.*, 1999; Smith *et al.*, 2011; Bevilacqua *et al.*, 2016). These were sampled to investigate relationships between eruption magnitude and apatite volatile compositions. The Baia–Fondi di Baia (B–FdB) and Monte Nuovo eruptions were sampled because they produced highly evolved melts from vents in the western NYT caldera. Baia–Fondi di Baia was the first eruption of Epoch 2 and was particularly explosive, owing to magma–H₂O phreatomagmatic interaction, but it expelled only a relatively small volume of material (Pistolesi *et al.*, 2017). The most evolved melts identified in Campi Flegrei were produced in the historical Monte Nuovo tuff cone eruption (Smith *et al.*, 2011). The latitic Santa Maria delle Grazie (SMdG) lava, which is thought to be part of a shallow dyke that fed the SMdG scoria cone (Isaia *et al.*, 2009), and the subsequent trachytic Accademia lava dome (Isaia *et al.*, 2009; Melluso *et al.*, 2012) were sampled to assess differences between apatite volatile compositions in these deposits and explosive units.

Samples

All samples were collected from proximal deposits (Fig. 1), either by Smith *et al.* (2011) or during fieldwork for this study in March 2013 and September 2014. Minopoli 1, PP, Pisani 1, B–FdB and Astroni 1 samples are CF13, CF6, CF25, CF88 and CF69 of Smith *et al.* (2011). The Astroni 1 sample was investigated by Stock *et al.* (2016). CF88 is from the initial fallout (Baia) phase of the B–FdB eruption (Pistolesi *et al.*, 2017). The Monte Nuovo sample (CF195) is from the upper pyroclastic flow unit (Table 1; Unit II of Piochi *et al.*, 2005). The SMdG (CF200) and Accademia (CF163) samples were collected from the centre of the NYT caldera.

Table 1: Summary of eruption deposits analysed, including age estimate, deposit characteristics (i.e. eruption style), erupted volume (i.e. magnitude estimate), average matrix glass composition, vent location and sampling location

Epoch	Eruption	Sample number	Age (cal. years BP)	Deposit type	Erupted volume (km ³)	Average matrix glass composition	Vent location*		Sampling location	
							UTM X	UTM Y	UTM X	UTM Y
	Monte Nuovo	CF195	1538 CE*	Pyroclastic density current deposit	~0.03*	Phonolite	423095	4520870	423277	4520614
Epoch 3	Astroni 1	CF69	4155–4357*	Ash fall with some lapilli layers	~0.06*	Phonolite	427999	4522122	428859*	4523584*
	Accademia Santa Maria delle Grazie	CF163	4205–4507* ¹	Lava dome	<0.01*	Trachyte [§]	427551	4519282	427597	4519562
		CF200	4383–4507*	Shallow feeder dyke	<0.01*	Latite	427625	4519806	427421	4518909
Epoch 2	Baia-Fondi di Baia	CF88	9525–9705*	Pumice fall	0.02–0.04 [†]	Trachyte	421855	4517930	421844*	4518253*
Epoch 1	Pisani 1	CF25	10516–12107* ²	Scoria fall	0.1–0.3*	Tephri-phonolite-trachy-andesite	428260	4523970	430237*	4525994*
	Pomici Principali	CF6	11907–12107*	Plinian fall (B3 unit)	0.43–1.28 [‡]	Tephri-phonolite-phonolite	428698	4522284	433890*	4522346*
	Minopoli 1	CF13	11907–12725* ³	Scoria fall	<0.1*	Phono-tephrite-tephri-phonolite	432400	4522670	432805*	4522632*

Erupted volumes are given as dense rock equivalent. Where exposure permitted, samples were collected vertically through volcanoclastic units and included both lapilli- and ash-sized material. The Pomici Principali sample represents only the B3 Plinian phase of the eruption and the Baia-Fondi di Baia sample comprises only the basal Baia fallout units. Samples from the deposits of these eruptions show only limited diversity in glass compositions (Smith *et al.*, 2011) and the analysed samples are therefore assumed representative of the bulk erupted material.

*Data from Smith *et al.* (2011). All ages of Smith *et al.* (2011) have been recalibrated using IntCal13 (Reimer *et al.*, 2013).

[†]Data from Pistolesi *et al.* (2017).

[‡]Data from Bevilacqua *et al.* (2016).

[§]Whole-rock composition from Melluso *et al.* (2012).

^{||}Whole-rock composition from Isaia *et al.* (2009).

¹Eruption not directly dated but stratigraphically older than the Solfatara eruption (4205–4427 years BP) and younger than Santa Maria delle Grazie.

²Eruption not directly dated but stratigraphically older than Pisani 3 (10 517–10 760 years BP) and younger than Pomici Principali.

³Eruption not directly dated but stratigraphically older than Pomici Principali and younger than Archiaverno (12 579–12 725 years BP).

All samples have the major phase assemblage K-feldspar + plagioclase + clinopyroxene + biotite + apatite + magnetite. Samples also contain fluorite ± sulphides ± sodalite ± leucite, with precipitation of these accessory phases constrained to late in magmatic evolution by their absence as phenocryst-hosted inclusions in natural samples, and by experimental studies and thermodynamic models (Fowler *et al.*, 2007; Arzilli *et al.*, 2016). Olivine is reported in mafic samples from Campi Flegrei (Cannatelli *et al.*, 2007) but was not observed in this study. Crystal contents are typically <5–30% (from qualitative observations and Isaia *et al.*, 2004; Piochi *et al.*, 2005; Mastrolorenzo & Pappalardo, 2006) but are notably lower in B-FdB (<1%; Mastrolorenzo & Pappalardo, 2006). In Monte Nuovo, two pyroxene populations can be identified in hand specimen: one black and one green, as in other eruptions at Campi Flegrei and Vesuvius (Cioni *et al.*, 1998; D'Antonio *et al.*, 1999). As apatite and melt inclusions show no systematic compositional difference between these pyroxene populations, they are not separated in the following discussion.

Analytical methods

Clinopyroxene and biotite phenocrysts were hand-picked from the 250–500 µm size fraction in samples from explosive eruptions and the Accademia lava

dome. Heavy liquid and magnetic separation techniques were used to extract apatite microphenocrysts from the 44–250 µm size fraction. Crystals and matrix ash grains were mounted in epoxy, ground and polished for analysis. Lava samples were prepared as polished thin sections. Samples were examined using an FEI Quanta 650 FEG scanning electron microscope (SEM), operating with a 20 kV, ~6–7 nA beam, in the Department of Earth Sciences, University of Oxford. Only apatite inclusions away from cracks and fully enclosed within host phenocrysts were analysed, to ensure that they were trapped during phenocryst growth and were unable to subsequently re-equilibrate with melt or fluids. Melt inclusions were analysed only if they did not show visual evidence for post-entrapment crystallization and were located away from cracks in their host phenocryst. Ash, lapilli fragments and lavas were also assessed by SEM to identify microlite-free regions for analysis of the matrix glass compositions.

Mineral and glass major, trace and halogen element compositions were analysed using a JEOL 8600 electron microprobe at the Research Laboratory for Archaeology and the History of Art, University of Oxford. Samples were re-polished prior to electron probe microanalysis (EPMA) to remove any compositional modification induced by SEM electron-beam exposure (Stock *et al.*, 2015), and subsequently carbon

coated along with secondary standards to avoid variable light element X-ray attenuation. Apatite was analysed using a defocused (5 μm), 15 kV, 10 nA beam, with halogens analysed first. Where possible, apatite crystals were analysed with the *c*-axis parallel to the plane of the mount. This routine limits the potential for time-dependent variability in halogen X-ray counts during analysis (Stormer *et al.*, 1993; Goldoff *et al.*, 2012; Stock *et al.*, 2015), while maintaining reasonable precision for low-concentration elements (i.e. Cl). In glass, most elements were measured using a defocused (10 μm), 15 kV, 6 nA beam to minimize Na_2O and SiO_2 migration (e.g. Humphreys *et al.*, 2006); when in low abundance, SO_2 , P_2O_5 and Cl were measured in a second analysis using a 30 nA current. In both crystals and glass, count times were 20–30 s for major elements and 30–90 s for minor elements (120 s for Cl and SO_2 in apatite). Backgrounds were determined by counting for half of the on-peak count time on either side of the peak. Glass and apatite analytical totals were typically 95–99% and 96–102%, respectively. Data were filtered to remove analyses with totals <92%, and >101.5% in glass. Apatite totals >100% probably reflect minor electron-beam induced compositional modification (Stock *et al.*, 2015) and totals significantly <100% probably result from the absence of trace elements [e.g. rare earth elements (REEs)] in the analytical routine. Apatite OH contents in EPMA data were calculated ‘by difference’, assuming stoichiometry. Typical analytical uncertainties are reported in Tables 2 and 3.

A subset of apatites and glasses was analysed by secondary ion mass spectrometry (SIMS) for H, F and Cl using a Cameca ims-4f system at the Edinburgh Ion Micro-Probe Facility, University of Edinburgh, using the methods outlined by Stock *et al.* (2016). Samples were re-polished prior to SIMS analysis to remove any surficial halogen modification induced during EPMA (Stock *et al.*, 2015). In apatite, F, Cl and H_2O concentrations were derived from working curves of $^{19}\text{F}/^{44}\text{Ca}$ vs F, $^{35}\text{Cl}/^{44}\text{Ca}$ vs Cl and $^1\text{H}/^{44}\text{Ca}$ vs H_2O , populated by independently characterized apatite standards (Supplementary Data Fig. S1; supplementary data are available for downloading at <http://www.petrology.oxfordjournals.org>). Glass H_2O concentrations were similarly derived from working curves of $^1\text{H}/^{30}\text{Si}$ vs H_2O populated by well-characterized rhyolitic glasses (Supplementary Data Fig. S2). Working curves were created at the beginning of each day, analytical session or when beam conditions were changed. NIST SRM610 was used as a primary standard for glass F calibration, with ^{44}Ca as the internal standard, based on EPMA of the same spot. SIMS backgrounds were monitored using anhydrous synthetic apatite or clinopyroxene crystals for apatite and glass, respectively. Working curves have a polynomial fit for H_2O in apatite and linear fit for all other elements, with R^2 typically >0.99. Typical analytical uncertainties are reported in Tables 2 and 3.

APATITE AND GLASS COMPOSITIONS

In total, >800 apatite and >250 glass analyses were acquired on samples from the eight Campi Flegrei eruptions (Table 1), using EPMA to identify broad compositional trends (full datasets are given in Supplementary Data Tables S1 and S2) and SIMS to measure a subset of crystals and glasses for H_2O and halogens with lower analytical uncertainties (Tables 2 and 3). All glass data in the text and Figs 2, 3 and 4a–d are plotted normalized to 100% anhydrous. All apatite analyses were made close to the centre of the mineral grains. Glass compositions could not be obtained from lava deposits (Table 1), owing to melt inclusion devitrification and groundmass crystallization. Apatite inclusions from these eruptions were excluded as they were not isolated from melt or fluids after entrapment: biotites are partially (in the case of SMdG) or fully (for Accademia) broken down and pyroxenes are heavily fractured, such that all apatite inclusions are touching major cracks or are incompletely enclosed by their host crystals. Baia-Fondi di Baia melt inclusions were too small (typically <20 μm) to analyse by SIMS. Astroni 1 apatite data from Stock *et al.* (2016) were recalibrated using updated standard compositions, resulting in minor modification of absolute compositions but no change to the trends in this dataset. These were included with additional glass and apatite analyses from this eruption.

Glass major element compositions

Melt inclusions and matrix glasses analysed in this study cover a wide compositional range from trachybasalts and basanites to phonolites and trachytes (Table 2; Supplementary Data Table S1), encompassing almost the entire compositional diversity reported in <15 ka Campi Flegrei deposits (Figs 2 and 3). Clinopyroxene-hosted melt inclusion compositions differ between eruptions: Minopoli 1 melt inclusions are the most mafic (50.46–56.84 wt % SiO_2) and cover the largest compositional range; Pisani 1 and PP include the next most mafic melt inclusions, with SiO_2 as low as 54.18 wt %; and melt inclusions from other eruptions are typically phonolitic to trachytic (Fig. 2). The same overall trend is seen for the matrix glasses (Fig. 3), although, in general, they are more evolved than melt inclusions from the same eruption, with higher SiO_2 (typically >53 wt %) and alkali element concentrations (Table 2; Supplementary Data Table S1).

For all elements measured, melt inclusion and matrix glass compositions plot on a single compositional trend, in agreement with literature data (Figs 2 and 3). Glass SiO_2 , Na_2O and K_2O concentrations typically increase with decreasing MgO, whereas CaO, FeO (all Fe as FeO) and TiO_2 concentrations decrease (Figs 2 and 3; Table 2; Supplementary Data Table S1). However, glass K_2O and SiO_2 concentrations decrease at low MgO contents (≤ 0.5 wt % MgO). Some low-MgO matrix glasses from Monte Nuovo and B-FdB are particularly K_2O -

Table 2: Major and volatile element analyses of representative Campi Flegrei glasses

Eruption:	Monte Nuovo	Monte Nuovo	Monte Nuovo	Monte Nuovo	Monte Nuovo	Monte Nuovo	Monte Nuovo	Monte Nuovo	Monte Nuovo	Monte Nuovo
Analysis #:	CF195_cp x113_m6	CF195_cp x64_m1	CF195_cp x86_m2	CF195_cp x86_m3	CF195_cp x110_m1	CF195_cp x113_m7	CF195_cp x122_m1	CF195_cp x122_m2	CF195_cp x123_m3	CF195_cp x137_m5
Type:	mi	mi	mi	mi	mi	mi	mi	mi	mi	mi
SiO ₂	58.77	57.35	57.81	56.19	58.05	57.63	58.35	58.26	59.68	58.71
Na ₂ O	4.45	4.04	4.11	3.94	5.04	4.65	4.20	4.08	5.03	4.42
MgO	0.55	0.77	0.75	0.74	0.76	0.59	0.87	0.81	0.51	0.70
Al ₂ O ₃	18.17	17.70	18.27	17.26	16.54	18.02	18.03	18.12	16.97	17.71
K ₂ O	8.40	8.57	8.49	7.89	6.86	8.37	8.48	8.94	7.43	8.42
CaO	2.22	2.59	2.55	2.48	2.72	2.26	2.81	2.83	2.33	2.24
TiO ₂	0.43	0.48	0.48	0.42	0.55	0.46	0.50	0.44	0.53	0.49
MnO	0.09	0.09	0.11	0.15	0.19	0.08	0.10	0.12	0.12	0.11
FeO _t	3.31	3.82	3.46	3.39	3.96	3.38	3.83	3.66	3.85	3.37
P ₂ O ₅	0.08	0.15	0.13	0.14	0.08	0.12	0.13	0.13	0.10	0.11
Cl	0.95	0.66	0.73	0.64	0.85	0.84	0.67	0.66	0.94	0.77
F	0.25	0.22	0.23	0.22	0.22	0.28	0.25	0.22	0.23	0.28
H ₂ O	2.82	3.48	2.84	5.56	3.47	2.45	2.44	1.04	2.28	2.54
Total	100.47	99.93	99.96	99.01	99.29	99.12	100.67	99.31	100.01	99.87
Eruption:	Monte Nuovo	Monte Nuovo	Monte Nuovo	Monte Nuovo	Monte Nuovo	Monte Nuovo	Monte Nuovo	Astroni 1	Astroni 1	Astroni 1
Analysis #:	CF195_cp x159_m4	CF195_cp x188_m1	VF55_cf19 5_1_1	VF55_cf19 5_2_1	VF55_cf19 5_3_1	VF55_cf19 5_4_1	VF55_cf19 5_4_2	CF69_cp x22_m1	CF69_cp x23_m2	CF69_cp x55_m1
Type:	mi	mi	mg	mg	mg	mg	mg	mi	mi	mi
SiO ₂	57.83	58.59	56.50	57.19	58.62	57.66	57.48	57.70	59.17	56.74
Na ₂ O	4.85	4.77	6.88	7.88	7.56	7.69	7.29	4.39	4.25	4.26
MgO	0.66	0.68	0.21	0.25	0.28	0.17	0.18	0.65	0.42	0.54
Al ₂ O ₃	17.10	17.52	18.28	18.79	19.04	18.69	18.87	17.90	17.84	18.07
K ₂ O	7.18	8.25	6.88	7.23	7.25	7.20	7.30	8.08	8.36	8.89
CaO	2.59	2.52	1.81	1.51	1.66	1.69	1.75	2.47	2.19	2.17
TiO ₂	0.50	0.47	0.49	0.50	0.39	0.45	0.43	0.45	0.49	0.41
MnO	0.20	0.13	0.24	0.37	0.20	0.20	0.28	0.10	0.19	0.04
FeO _t	3.91	3.38	3.08	3.30	2.74	2.89	3.19	3.36	3.65	3.15
P ₂ O ₅	0.15	0.11	0.01	0.00	0.00	0.05	0.07	0.12	0.10	0.08
Cl	0.89	0.78	0.90	0.97	0.97	1.05	1.17	0.96	1.00	0.87
F	0.24	0.32	1.21	0.65	0.73	0.82	0.68	0.28	0.28	0.26
H ₂ O	3.71	2.38	0.88	0.76	0.97	1.06	1.08	2.37	2.22	2.12
Total	99.80	99.88	97.36	99.41	100.41	99.60	99.77	98.82	100.15	97.60
Eruption:	Astroni 1	Astroni 1	Astroni 1	Astroni 1	Astroni 1	Astroni 1	Astroni 1	Astroni 1	Astroni 1	Astroni 1
Analysis #:	CF69_cpx 55_m2	CF69_cpx 66_m1	CF69_cpx 66_m3	CF69_cpx 82_m1	CF69_cpx 91_m1	CF69_cpx 92_m1	CF69_cpx 97_m3	CF69_cpx 113_m1	CF69_cpx 116_m1	CF69_cpx 127_m1
Type:	mi	mi	mi	mi	mi	mi	mi	mi	mi	mi
SiO ₂	56.99	54.97	56.56	56.78	58.21	57.38	57.73	56.74	56.44	56.55
Na ₂ O	4.52	4.15	4.02	4.20	4.60	4.35	4.46	4.76	3.65	4.22
MgO	0.53	0.61	0.72	0.50	0.51	0.76	0.54	0.55	0.78	0.58
Al ₂ O ₃	17.82	17.60	18.24	17.90	17.67	18.60	17.91	17.51	18.40	17.65
K ₂ O	8.50	8.55	8.83	8.35	8.37	8.44	8.27	8.57	8.84	8.28
CaO	2.15	2.43	2.62	2.07	2.03	2.47	2.34	2.17	2.37	2.34
TiO ₂	0.44	0.47	0.47	0.45	0.48	0.41	0.45	0.45	0.51	0.45
MnO	0.13	0.09	0.12	0.19	0.20	0.11	0.12	0.15	0.02	0.10
FeO _t	3.37	3.76	4.20	3.40	3.40	2.85	3.38	3.19	3.27	3.84
P ₂ O ₅	0.10	0.14	0.13	0.13	0.08	0.17	0.08	0.08	0.15	0.15
Cl	0.93	0.75	0.69	0.91	1.03	0.84	0.90	0.93	0.73	0.82
F	0.25	0.21	0.23	0.28	0.31	0.30	0.25	0.25	0.22	0.20
H ₂ O	2.56	2.21	2.58	2.29	2.27	2.21	2.00	2.62	2.33	2.51
Total	98.28	95.94	99.41	97.46	99.16	98.90	98.43	97.97	97.71	97.70
Eruption:	Astroni 1	Astroni 1	Astroni 1	Astroni 1	Astroni 1	Astroni 1	Astroni 1	Astroni 1	Astroni 1	Astroni 1
Analysis #:	CF69_cpx 127_m3	CF69_cpx 130_m1	CF69_cpx 138_m2	CF69_cpx 156_m2	CF69_cpx 182_m1	CF69_cpx 182_m2	VF55_cf69 2_1	VF55_cf69 3_1	VF55_cf69 5_1	VF55_cf69 6_1
Type:	mi	mi	mi	mi	mi	mi	mg	mg	mg	mg
SiO ₂	57.17	56.80	55.39	58.52	55.35	55.59	59.14	57.69	59.43	58.83
Na ₂ O	4.07	4.51	4.62	4.56	3.76	3.87	3.90	4.38	4.67	4.50
MgO	0.54	0.55	0.42	0.45	0.71	0.77	0.54	0.50	0.49	0.58
Al ₂ O ₃	17.63	17.67	17.09	17.12	17.52	17.53	18.37	17.85	18.09	18.11
K ₂ O	8.36	8.37	8.48	8.03	8.53	8.48	8.61	8.47	8.44	8.56
CaO	2.31	2.30	2.01	2.23	2.64	2.70	2.29	2.28	2.45	2.36
TiO ₂	0.49	0.51	0.40	0.48	0.48	0.50	0.48	0.42	0.46	0.37
MnO	0.14	0.11	0.13	0.16	0.12	0.17	0.16	0.17	0.16	0.07
FeO _t	3.60	3.40	3.34	3.53	3.90	3.39	3.27	3.31	3.42	3.41
P ₂ O ₅	0.16	0.10	0.06	0.09	0.20	0.12	0.04	0.09	0.09	0.05
Cl	0.88	0.93	0.97	0.91	0.74	0.73	0.91	0.91	0.94	0.92
F	0.20	0.28	0.27	0.26	0.19	0.21	0.25	0.26	0.22	0.25
H ₂ O	2.57	2.43	2.69	2.30	2.39	2.51	0.71	0.67	0.20	1.26
Total	98.12	97.95	95.85	98.63	96.52	96.58	98.67	96.99	99.06	99.27

(continued)

Table 2: Continued

Eruption:	Astroni 1	Astroni 1	Astroni 1	Baia-Fondi	Pisani 1	Pisani 1	Pisani 1	Pisani 1	Pisani 1	Pisani 1
Analysis #:	VF55_cf69	VF55_cf69	VF55_cf69	di Baia VF55	CF25_cpx	CF25_cpx	CF25_cpx	CF25_cpx	CF25_cpx	CF25_cpx
Type:	_8_1 mg	_9_1 mg	_9_2 mg	_cf88_1_2 mg	86_m3 mi	129_m3 mi	54_m3 mi	118_m3 mi	129_m1 mi	129_m2 mi
SiO ₂	58.84	56.79	58.68	58.39	52.97	55.86	55.81	52.47	57.52	55.12
Na ₂ O	4.26	2.87	4.52	4.95	3.53	3.36	3.46	3.55	3.57	3.55
MgO	0.48	0.52	0.59	0.34	1.34	1.00	1.17	1.05	0.97	1.07
Al ₂ O ₃	18.19	18.09	18.01	16.03	17.97	17.53	17.89	17.60	18.25	18.01
K ₂ O	8.65	8.09	8.67	6.79	8.20	8.14	7.88	7.70	7.98	7.99
CaO	2.10	2.41	2.49	2.14	3.43	3.57	3.58	3.65	3.57	3.58
TiO ₂	0.40	0.48	0.45	0.54	0.62	0.59	0.63	0.64	0.58	0.56
MnO	0.18	0.14	0.20	0.26	0.02	0.21	0.10	0.13	0.22	0.22
FeOt	3.06	3.37	3.33	4.29	4.70	4.76	4.91	5.03	5.23	5.07
P ₂ O ₅	0.09	0.10	0.13	0.05	0.45	0.24	0.25	0.28	0.18	0.21
Cl	0.86	0.85	0.92	1.15	0.60	0.69	0.78	0.71	0.77	0.83
F	0.09	0.26	0.29	0.23	0.19	0.19	0.21	0.23	0.24	0.23
H ₂ O	0.63	0.91	0.95	0.77	2.17	2.23	2.37	2.30	2.12	2.32
Total	97.83	94.89	99.23	95.92	96.17	98.39	99.04	95.35	101.22	98.75
Eruption:	Pisani 1	Pisani 1	Pisani 1	Pisani 1	Pomici	Pomici	Pomici	Pomici	Pomici	Pomici
Analysis #:	VF55_cf25	VF55_cf25	VF55_cf25	VF55_cf25	Principali	Principali	Principali	Principali	Principali	Principali
Type:	_2_1a mg	_2_1b mg	_4_1 mg	_4_2 mg	CF6_cpx	CF6_cpx	CF6_cpx	CF6_cpx	CF6_cpx	CF6_cpx
					29_m1 mi	98_m1 mi	110_m1 mi	121_m2 mi	192_m1 mi	_137_2 mi
SiO ₂	56.27	56.27	55.42	54.66	57.09	56.58	56.59	57.57	57.05	56.34
Na ₂ O	3.34	3.34	3.08	3.17	4.06	3.70	3.83	3.39	3.24	3.95
MgO	1.53	1.53	2.08	1.96	0.82	0.83	0.54	0.77	0.72	0.54
Al ₂ O ₃	17.82	17.82	17.90	18.21	18.24	18.19	18.21	18.45	18.11	18.15
K ₂ O	8.13	8.13	7.11	7.27	9.28	9.22	9.18	9.08	8.84	9.10
CaO	4.27	4.27	5.52	5.35	3.16	3.18	2.95	3.17	3.14	3.06
TiO ₂	0.65	0.65	0.75	0.81	0.41	0.45	0.47	0.48	0.46	0.55
MnO	0.09	0.09	0.13	0.06	0.09	0.16	0.17	0.04	0.14	0.14
FeOt	5.41	5.41	6.21	6.07	3.67	3.92	3.94	3.82	3.89	3.90
P ₂ O ₅	0.42	0.42	0.50	0.49	0.14	0.14	0.17	0.12	0.12	0.11
Cl	0.76	0.76	0.56	0.61	0.74	0.73	0.67	0.73	0.72	0.86
F	0.22	0.20	0.31	0.27	0.23	0.22	0.25	0.22	0.28	0.24
H ₂ O	0.14	0.14	0.05	0.33	1.26	3.84	2.52	1.98	3.35	2.35
Total	99.06	99.04	99.63	99.26	99.21	101.16	99.47	99.82	100.05	99.30
Eruption:	Pomici	Pomici	Pomici	Pomici	Pomici	Pomici	Minopoli 1	Minopoli 1	Minopoli 1	Minopoli 1
Analysis #:	Principali	Principali	Principali	Principali	Principali	Principali	CF13_cpx	CF13_cpx	CF13_cpx	CF13_cpx
Type:	CF6_cpx	VF55_cf6	VF55_cf6	VF55_cf6	VF55_cf6	VF55_cf6	29_m1 mi	142_m1 mi	_140_1 mi	_135_1 mi
	_167_1 mi	_1_1 mg	_1_2 mg	_1_3 mg	_1_4 mg	_1_6 mg				
SiO ₂	56.56	56.31	55.90	56.52	55.79	56.16	49.19	49.92	53.36	54.30
Na ₂ O	3.54	3.71	3.21	3.25	3.45	3.67	2.61	3.54	2.36	3.44
MgO	0.83	1.03	0.92	0.98	1.03	1.00	3.26	2.23	3.56	2.07
Al ₂ O ₃	18.41	17.98	17.96	18.45	17.74	17.99	18.29	18.30	16.98	18.35
K ₂ O	9.00	8.90	8.94	9.16	9.00	8.98	5.78	7.45	5.82	7.62
CaO	3.17	3.64	3.43	3.68	3.86	3.69	7.30	5.83	6.35	5.35
TiO ₂	0.44	0.45	0.47	0.47	0.50	0.42	0.98	0.86	0.66	0.83
MnO	0.17	0.13	0.19	0.12	0.04	0.17	0.12	0.17	0.11	0.14
FeOt	3.56	4.24	4.13	4.18	4.18	4.24	7.42	7.02	4.85	4.82
P ₂ O ₅	0.15	0.17	0.12	0.16	0.22	0.14	0.66	0.63	0.68	0.63
Cl	0.84	0.69	0.75	0.71	0.69	0.73	0.48	0.51	0.59	0.77
F	0.27	0.24	0.27	0.26	0.24	0.14	0.29	0.30	0.28	0.22
H ₂ O	2.69	0.32	0.10	1.10	0.33	0.35	1.87	1.30	3.05	1.25
Total	99.63	97.82	96.39	99.03	97.07	97.69	98.25	98.06	98.64	99.80
Eruption:	Minopoli 1	Minopoli 1	Minopoli 1	Minopoli 1	Minopoli 1	Minopoli 1	Minopoli 1	Minopoli 1		RP
Analysis #:	CF13_cpx	CF13_cpx	CF13_cpx	VF55_cf13	VF55_cf13	VF55_cf13	VF55_cf13	VF55_cf13		
Type:	_55_1 mi	_49_2 mi	119_m1 mi	_1_2 mg	_3_1 mg	_4_1 mg	_5_1 mg	_10_1 mg		
SiO ₂	52.65	49.23	48.34	53.43	53.34	49.92	53.38	53.01		0.42
Na ₂ O	2.96	2.40	2.32	3.15	2.91	3.01	2.96	2.87		0.26
MgO	2.29	3.62	3.57	2.35	2.40	2.19	2.14	2.28		0.06
Al ₂ O ₃	17.30	17.53	17.55	16.79	17.06	15.73	18.49	17.27		0.23
K ₂ O	6.50	5.09	4.88	7.17	7.47	6.65	6.64	6.67		0.20
CaO	5.63	7.79	7.51	5.82	5.65	5.47	6.27	5.82		0.12
TiO ₂	0.92	0.98	0.83	1.04	1.01	0.97	0.92	0.95		0.08
MnO	0.18	0.20	0.18	0.19	0.18	0.13	0.17	0.25		0.09
FeOt	6.90	7.93	7.82	6.98	6.94	6.74	7.02	7.32		0.25
P ₂ O ₅	0.44	0.65	0.70	0.68	0.76	0.59	0.59	0.67		0.02
Cl	0.67	0.55	0.55	0.63	0.55	0.73	0.50	0.62		0.06
F	0.33	0.44	0.31	0.31	0.29	0.30	0.34	0.33		0.01
H ₂ O	2.26	2.53	2.63	0.14	0.14	0.14	0.21	0.08		0.37
Total	99.03	98.92	97.19	98.69	98.71	92.58	99.61	98.13		

F and H₂O were measured by SIMS; all other elements were measured by EPMA. Analysis type refers to textural association: mi, melt inclusion; mg, matrix glass. Concentrations are in wt %. RP is representative absolute precision with 1SD based on counting statistics for F and elements measured by EPMA, and a 95% confidence interval based on regression of calibration standards for H₂O.

Table 3: Major and volatile element analyses of representative Campi Flegrei apatite inclusions and microphenocrysts

Eruption:	Monte Nuovo	Monte Nuovo	Monte Nuovo	Monte Nuovo	Monte Nuovo	Monte Nuovo	Monte Nuovo	Monte Nuovo	Monte Nuovo	Monte Nuovo
Crystal #:	CFmap2_C F195_19	CFmap2_C F195_16	CFmap2_C F195_17	CFmap2_C F195_8	CFmap2_C F195_49	CFmap2_C F195_38	CFmap2_C F195_35	CFmap2_C F195_30	CFmap2_C F195_24	CFmap2_C F195_22
Type:	mpc	mpc	mpc	mpc	mpc	mpc	mpc	mpc	mpc	mpc
P ₂ O ₅	38.91	41.20	41.37	41.38	41.63	40.09	41.37	41.34	40.92	40.93
SiO ₂	1.60	0.58	0.40	0.42	0.66	0.85	0.44	0.58	0.55	0.69
CaO	53.97	54.09	54.28	54.00	53.42	52.59	53.49	54.32	53.79	53.28
SO ₂	1.34	0.70	0.42	0.41	0.14	0.63	0.42	0.19	0.56	0.44
F	2.30	2.03	2.03	2.13	2.83	2.08	2.09	2.58	2.29	2.56
Cl	0.07	0.92	0.90	0.93	0.88	1.02	0.91	0.86	1.04	0.89
OH	1.57	1.09	1.08	1.20	0.57	1.19	1.13	0.57	0.75	0.66
O ≡ F, Cl, OH	1.72	1.58	1.57	1.67	1.66	1.67	1.62	1.55	1.55	1.59
Total	98.04	99.03	98.91	98.80	98.47	96.78	98.23	98.89	98.35	97.86
Eruption:	Monte Nuovo	Monte Nuovo	Monte Nuovo	Monte Nuovo	Monte Nuovo	Monte Nuovo	Monte Nuovo	Monte Nuovo	Monte Nuovo	Monte Nuovo
Crystal #:	CFmap2_C F195_45	CFmap2_C F195_31	CFmap2_C F195_12	CFmap2_C F195_97	CFmap2_C F195_46	CFmap2_C F195_64	CFmap2_C F195_74	CFmap2_C F195_98	CF195_cpx 63_ap1	CF195_cpx 80_ap4
Type:	mpc	mpc	mpc	mpc	mpc	mpc	mpc	mpc	cpx	cpx
P ₂ O ₅	40.97	40.47	41.32	40.99	41.39	41.06	40.36	41.36	41.29	41.35
SiO ₂	0.68	1.32	0.61	0.54	0.41	0.43	0.90	0.63	0.61	0.50
CaO	53.20	52.93	53.68	54.32	53.37	54.19	53.78	54.67	53.85	54.13
SO ₂	0.25	0.17	0.56	0.23	0.27	0.42	0.13	0.16	0.39	0.36
F	2.28	2.02	2.47	2.36	2.50	2.08	2.94	3.30	2.12	2.35
Cl	1.05	0.94	0.98	1.04	0.89	1.04	0.54	0.12	0.98	0.92
OH	1.02	1.23	0.48	0.70	0.55	0.94	0.49	0.17	0.62	0.45
O ≡ F, Cl, OH	1.68	1.64	1.49	1.56	1.51	1.55	1.59	1.50	1.41	1.41
Total	97.77	97.44	98.61	98.62	97.87	98.61	97.55	98.91	98.44	98.64
Eruption:	Monte Nuovo	Monte Nuovo	Monte Nuovo	Monte Nuovo	Monte Nuovo	Monte Nuovo	Monte Nuovo	Monte Nuovo	Monte Nuovo	Monte Nuovo
Crystal #:	CF195_cpx 83_ap3	CF195_cpx 80_ap1	CF195_cpx 128_ap1	CF195_cpx 128_ap4	CF195_cpx 133_ap1	CF195_cpx 137_ap1	CF195_cpx 173_ap1	CF195_cpx 121_ap1	CF195_cpx 188_ap1	CF195_cpx 208_ap1
Type:	cpx	cpx	cpx	cpx	cpx	cpx	cpx	cpx	cpx	cpx
P ₂ O ₅	41.93	41.30	40.73	41.02	40.57	40.96	39.65	40.21	40.89	40.80
SiO ₂	0.37	0.45	0.79	0.72	0.48	0.60	1.32	0.67	0.67	0.76
CaO	53.36	53.87	53.18	53.80	53.63	53.84	53.03	53.76	53.94	54.25
SO ₂	0.21	0.36	0.34	0.25	0.57	0.55	0.12	0.49	0.40	0.50
F	2.23	2.35	2.30	2.36	2.07	2.51	2.06	2.52	2.53	2.00
Cl	0.94	0.91	1.00	0.79	0.97	0.92	0.91	0.92	0.79	0.91
OH	0.47	0.45	0.53	0.52	0.67	0.46	0.84	0.46	0.39	0.74
O ≡ F, Cl, OH	1.37	1.41	1.44	1.42	1.40	1.48	1.46	1.48	1.43	1.39
Total	98.13	98.29	97.42	98.05	97.56	98.35	96.47	97.54	98.19	98.57
Eruption:	Monte Nuovo	Monte Nuovo	Monte Nuovo	Monte Nuovo	Astroni 1	Astroni 1	Astroni 1	Astroni 1	Astroni 1	Astroni 1
Crystal #:	CF195_cpx 250_ap4	CF195_bt40_ap1	CF195_bt46_ap1	CF195_bt64_ap3	CFmap2_CF69_47	CFmap2_CF69_32	CFmap2_CF69_29	CFmap2_CF69_10	CFmap2_CF69_26	CFmap2_CF69_6
Type:	cpx	bt	bt	bt	mpc	mpc	mpc	mpc	mpc	mpc
P ₂ O ₅	38.59	40.83	39.77	41.62	41.50	40.85	42.62	41.65	41.26	41.40
SiO ₂	1.46	0.80	0.52	0.54	0.64	0.80	0.06	0.61	0.76	0.56
CaO	52.53	53.12	53.90	53.72	54.55	52.57	53.77	53.38	53.59	53.84
SO ₂	1.16	0.32	0.34	0.36	0.39	0.10	0.15	0.45	0.22	0.63
F	2.38	2.36	2.41	2.48	3.16	2.58	2.59	2.68	2.56	2.49
Cl	0.93	1.03	0.87	0.91	0.53	1.06	0.94	0.92	0.96	0.96
OH	0.43	0.74	0.63	0.56	0.29	0.70	0.73	0.71	0.77	0.74
O ≡ F, Cl, OH	1.41	1.58	1.51	1.51	1.59	1.65	1.65	1.67	1.66	1.61
Total	96.07	97.63	96.93	98.68	99.47	97.01	99.21	98.73	98.46	99.01
Eruption:	Astroni 1	Astroni 1	Astroni 1	Astroni 1	Astroni 1	Astroni 1	Astroni 1	Astroni 1	Astroni 1	Astroni 1
Crystal #:	CFmap2_C F69_19	CFmap2_C F69_22	CFmap2_C F69_20	CFmap2_C F69_21	CFmap2_C F69_49	CFmap2_C F69_46	CFmap2_C F69_91	CFmap2_C F69_85	CFmap2_C F69_2	CFmap2_C F69_82
Type:	mpc	mpc	mpc	mpc	mpc	mpc	mpc	mpc	mpc	mpc
P ₂ O ₅	41.16	42.17	41.16	41.78	40.05	41.46	40.65	40.64	41.64	41.08
SiO ₂	0.67	0.61	0.66	0.62	1.10	0.68	0.64	0.65	0.61	0.74
CaO	53.39	53.78	53.77	53.98	53.01	53.35	53.79	53.86	54.23	53.95
SO ₂	0.14	0.16	0.45	0.28	0.18	0.17	0.15	0.69	0.29	0.15
F	2.49	2.51	2.42	2.43	2.61	2.33	2.01	2.56	2.50	2.48
Cl	0.97	0.93	0.95	0.94	1.01	0.99	1.07	0.99	0.98	1.01
OH	0.76	0.77	0.77	0.77	0.79	0.81	0.80	0.57	0.62	0.65
O ≡ F, Cl, OH	1.62	1.63	1.60	1.60	1.70	1.59	1.46	1.57	1.57	1.58
Total	97.96	99.30	98.58	99.20	97.05	98.20	97.65	98.39	99.30	98.48

(continued)

Table 3: Continued

Eruption: Crystal #:	Astroni 1 CFmap2_C F69_18 mpc	Astroni 1 CFmap2_C F69_74 mpc	Astroni 1 CF69_cpx 10_ap2 cpx	Astroni 1 CF69_cpx 11_ap1 cpx	Astroni 1 CF69_cpx 32_ap1 cpx	Astroni 1 CF69_cpx 35_ap1 cpx	Astroni 1 CF69_cpx 69_ap1 cpx	Astroni 1 CF69_cpx 73_ap2 cpx	Astroni 1 CF69_cpx 95_ap2 cpx	Astroni 1 CF69_cpx 104_ap1 cpx
Type:										
P ₂ O ₅	41.04	41.01	41.31	40.99	41.30	41.68	41.24	41.07	40.95	40.50
SiO ₂	0.57	0.64	0.68	0.76	0.77	0.66	0.68	0.82	0.67	0.78
CaO	53.67	54.30	54.05	53.92	54.36	54.34	54.09	53.78	53.81	53.95
SO ₂	0.40	0.22	0.09	0.32	0.30	0.29	0.15	0.24	0.24	0.29
F	2.57	2.30	2.32	2.13	2.22	2.40	2.36	2.30	2.33	2.34
Cl	1.01	0.57	0.90	0.99	0.92	0.91	0.91	0.88	0.89	0.89
OH	0.60	1.24	0.42	0.58	0.60	0.50	0.53	0.52	0.49	0.47
O ≡ F, Cl, OH	1.59	1.68	1.37	1.40	1.42	1.45	1.45	1.41	1.41	1.41
Total	98.27	98.60	98.38	98.29	99.05	99.33	98.51	98.20	97.96	97.81
Eruption: Crystal #:	Astroni 1 cpx110_ ap1 cpx	Astroni 1 CF69_cpx 132_ap1 cpx	Astroni 1 CF69_cpx 137_ap1 cpx	Astroni 1 CF69_cpx 139_ap2 cpx	Astroni 1 CF69_cpx 153_ap2 cpx	Astroni 1 CF69_cpx 151_ap1 cpx	Astroni 1 CF69_cpx 112_ap1 cpx	Astroni 1 CF69_cpx 65_ap2 cpx	Astroni 1 CF69_cpx 21_ap2 cpx	Astroni 1 CF69_cpx 44_ap6 cpx
Type:										
P ₂ O ₅	41.28	41.13	41.24	41.33	41.18	40.57	41.39	41.33	41.36	40.94
SiO ₂	0.64	0.61	0.61	0.57	0.59	0.94	0.50	0.72	0.55	0.56
CaO	53.31	53.37	53.72	54.14	53.71	53.52	54.33	54.62	54.03	53.97
SO ₂	0.12	0.38	0.32	0.18	0.33	0.15	0.47	0.17	0.25	0.46
F	2.25	1.86	2.35	2.46	2.22	2.31	2.36	2.45	2.30	2.30
Cl	0.96	0.88	0.89	0.87	1.00	0.92	0.91	0.91	0.96	0.86
OH	0.51	0.46	0.58	0.52	0.68	0.56	0.56	0.58	0.43	0.53
O ≡ F, Cl, OH	1.40	1.20	1.46	1.48	1.48	1.44	1.46	1.51	1.39	1.41
Total	97.67	97.48	98.24	98.59	98.22	97.53	99.06	99.27	98.50	98.21
Eruption: Crystal #:	Astroni 1 CF69_cpx 73_ap2 cpx	Astroni 1 CF69_bt 23_ap2 bt	Astroni 1 CF69_bt 23_ap3 bt	Astroni 1 CF69_bt 38_ap3 bt	Astroni 1 CF69_bt 48_ap1 bt	Astroni 1 CF69_bt 97_ap1 bt	Astroni 1 CF69_bt 117_ap1 bt	Astroni 1 CF69_bt 156_ap1 bt	Astroni 1 CF69_bt 167_ap1 bt	Astroni 1 CF69_bt 35_ap1 bt
Type:										
P ₂ O ₅	41.07	41.60	41.18	41.09	41.14	41.32	41.55	40.85	40.13	41.64
SiO ₂	0.82	0.56	0.59	0.69	0.59	0.60	0.53	0.51	0.59	0.47
CaO	53.78	53.97	54.18	53.86	54.14	54.30	54.51	54.49	53.81	54.06
SO ₂	0.24	0.34	0.38	0.58	0.31	0.56	0.38	0.40	0.35	0.42
F	2.34	2.40	2.49	2.52	2.42	2.40	2.54	2.37	2.40	2.43
Cl	0.94	0.90	0.93	0.93	0.90	0.92	0.96	0.91	0.88	0.89
OH	0.56	0.59	0.65	0.55	0.66	0.58	0.65	0.57	0.57	0.59
O ≡ F, Cl, OH	1.46	1.49	1.56	1.53	1.53	1.49	1.59	1.47	1.48	1.50
Total	98.29	98.89	98.85	98.68	98.62	99.19	99.53	98.63	97.26	99.00
Eruption: Crystal #:	Astroni 1 CF69_bt 27_ap1 bt	Astroni 1 CF69_bt 149_ap1 bt	Astroni 1 CF69_bt 98_ap1 bt	Astroni 1 CF69_bt 164_ap5 bt	Astroni 1 CF69_bt 164_ap1 bt	Astroni 1 CF69_bt 158_ap1 bt	Astroni 1 CF69_bt 170_ap1 bt	Accademia CFmap2_C F163_14 mpc	Accademia CFmap2_C F163_5 mpc	Accademia CFmap2_C F163_42 mpc
Type:										
P ₂ O ₅	41.78	40.49	40.98	40.95	41.25	41.75	40.97	41.50	40.93	39.97
SiO ₂	0.50	0.74	0.58	0.60	0.65	0.45	0.40	0.68	0.51	1.19
CaO	53.99	54.37	53.87	54.35	54.54	54.59	54.01	54.24	53.55	54.42
SO ₂	0.29	0.27	0.54	0.27	0.28	0.44	0.40	0.24	0.44	1.01
F	2.38	2.43	2.42	2.48	2.53	2.40	2.40	2.96	3.26	2.22
Cl	0.89	0.90	0.91	0.91	0.93	0.92	0.91	0.66	0.48	0.06
OH	0.53	0.65	0.53	0.66	0.64	0.53	0.53	0.21	0.07	1.62
O ≡ F, Cl, OH	1.45	1.53	1.48	1.56	1.58	1.47	1.46	1.49	1.51	1.71
Total	98.92	98.32	98.36	98.65	99.25	99.61	98.15	99.00	97.73	98.78
Eruption: Crystal #:	Accademia CFmap2_C F163_25 mpc	Accademia CFmap2_C F163_24 mpc	Accademia CFmap2_C F163_28 mpc	Accademia CFmap2_C F163_20 mpc	Accademia CFmap2_C F163_46 mpc	Accademia CFmap2_C F163_39 mpc	Accademia CFmap2_C F163_32 mpc	Accademia CFmap2_C F163_8 mpc	Accademia CFmap2_C F163_6 mpc	Accademia CFmap2_C F163_11 mpc
Type:										
P ₂ O ₅	40.90	41.38	41.20	40.94	41.73	40.88	41.21	40.93	40.99	40.68
SiO ₂	0.57	0.66	0.77	0.63	0.35	0.77	0.62	0.57	0.58	0.67
CaO	54.08	54.08	53.47	53.47	53.90	53.81	53.64	53.72	53.68	53.35
SO ₂	0.54	0.27	0.22	0.17	0.35	0.14	0.16	0.65	0.33	0.25
F	3.62	2.54	2.49	2.61	2.53	2.62	2.52	2.32	2.64	2.63
Cl	0.06	1.04	0.97	1.17	0.89	0.95	0.96	0.89	0.88	1.17
OH	0.01	0.48	0.56	0.36	0.41	0.54	0.56	0.59	0.45	0.51
O ≡ F, Cl, OH	1.54	1.53	1.53	1.53	1.46	1.57	1.54	1.46	1.52	1.61
Total	98.24	98.92	98.15	97.82	98.70	98.14	98.13	98.21	98.03	97.65

(continued)

Table 3: Continued

Eruption:	Accademia	Accademia	Accademia	Accademia	Accademia	Accademia	Accademia	Santa Maria delle Grazie	Santa Maria delle Grazie	Santa Maria delle Grazie
Crystal #:	CFmap2_C F163_10	mpc_C F163_10	mpc_C F163_9	mpc_C F163_8	CFmap2_C F163_100	CFmap2_C F163_63	CFmap2_C F163_12	CF200_map30	CF200_map29	CF200_map35
Type:	mpc	mpc	mpc	mpc	mpc	mpc	mpc	mpc	mpc	mpc
P ₂ O ₅	40.51	41.44	40.36	41.10	41.06	41.15	41.37	40.65	40.71	39.27
SiO ₂	0.76	0.61	0.82	0.67	0.77	0.60	0.53	0.66	0.61	1.53
CaO	53.20	54.41	53.97	54.22	54.29	54.37	53.97	54.06	53.94	52.93
SO ₂	0.23	0.17	0.10	0.23	0.13	0.31	0.16	0.46	0.37	0.24
F	2.83	3.29	3.69	3.78	3.79	3.77	3.60	2.85	3.54	2.67
Cl	0.92	0.09	0.06	0.10	0.05	0.05	0.07	0.68	0.23	1.04
OH	0.46	0.00	0.00	0.00	0.00	0.00	0.00	0.18	0.00	0.33
O = F, Cl, OH	1.62	1.41	1.57	1.61	1.61	1.60	1.53	1.44	1.54	1.51
Total	97.29	98.60	97.43	98.49	98.48	98.65	98.17	98.10	97.86	96.50
Eruption:	Santa Maria delle Grazie	Baia-Fondi di Baia	Baia-Fondi di Baia	Baia-Fondi di Baia	Baia-Fondi di Baia	Baia-Fondi di Baia	Baia-Fondi di Baia	Baia-Fondi di Baia	Baia-Fondi di Baia	Baia-Fondi di Baia
Crystal #:	CF200_map36	CFmap1_C F88_42	CFmap1_C F88_49	CFmap1_C F88_34	CFmap1_C F88_16	CFmap1_C F88_11	CFmap1_C F88_10	CFmap1_C F88_18	CFmap1_C F88_33	CFmap1_C F88_43
Type:	mpc	mpc	mpc	mpc	mpc	mpc	mpc	mpc	mpc	mpc
P ₂ O ₅	41.14	39.99	40.97	41.23	40.52	40.42	39.43	41.07	39.95	40.29
SiO ₂	0.59	0.49	0.50	0.42	0.61	0.54	1.02	0.60	0.94	0.79
CaO	53.86	53.95	54.14	53.98	54.01	54.05	53.80	53.64	52.89	53.19
SO ₂	0.33	0.39	0.34	0.43	0.20	0.39	0.90	0.16	0.56	0.13
F	3.57	2.06	2.07	2.29	2.10	2.17	2.18	1.99	1.98	2.32
Cl	0.09	0.85	0.89	0.87	0.86	0.78	0.72	0.87	0.86	0.91
OH	0.00	0.90	1.01	0.95	0.97	0.82	0.88	0.82	0.83	0.91
O = F, Cl, OH	1.52	1.48	1.55	1.61	1.53	1.48	1.49	1.42	1.42	1.61
Total	98.06	97.15	98.37	98.56	97.74	97.69	97.44	97.73	96.59	96.93
Eruption:	Baia-Fondi di Baia	Baia-Fondi di Baia	Baia-Fondi di Baia	Baia-Fondi di Baia	Baia-Fondi di Baia	Baia-Fondi di Baia	Baia-Fondi di Baia	Baia-Fondi di Baia	Baia-Fondi di Baia	Baia-Fondi di Baia
Crystal #:	CFmap1_C F88_30	CFmap1_C F88_3	CFmap1_C F88_8	CFmap1_C F88_50	CFmap1_C F88_44	CFmap1_C F88_31	CFmap1_C F88_45	CFmap1_C F88_22	CFmap1_C F88_17	CFmap1_C F88_12
Type:	mpc	mpc	mpc	mpc	mpc	mpc	mpc	mpc	mpc	mpc
P ₂ O ₅	41.05	41.61	40.04	39.79	40.04	38.69	40.03	39.84	39.93	40.03
SiO ₂	0.40	0.00	0.79	0.86	0.80	1.40	1.00	1.15	1.20	0.97
CaO	54.35	55.46	54.43	53.96	54.28	54.42	53.65	53.36	52.64	53.86
SO ₂	0.40	0.00	0.89	0.85	0.77	1.38	0.05	0.48	0.03	0.52
F	2.00	2.50	2.77	2.80	2.34	2.57	3.02	2.69	2.77	2.56
Cl	0.89	0.03	0.09	0.09	0.06	0.04	0.42	0.62	0.55	0.61
OH	0.88	0.92	0.93	0.79	1.16	0.97	0.47	0.63	0.68	0.59
O = F, Cl, OH	1.46	1.49	1.62	1.57	1.54	1.55	1.59	1.57	1.61	1.49
Total	98.51	99.03	98.32	97.57	97.91	97.92	97.05	97.20	96.19	97.65
Eruption:	Baia-Fondi di Baia	Baia-Fondi di Baia	Baia-Fondi di Baia	Baia-Fondi di Baia	Baia-Fondi di Baia	Baia-Fondi di Baia	Baia-Fondi di Baia	Pisani 1	Pisani 1	Pisani 1
Crystal #:	CFmap1_C F88_1	CFmap1_C F88_7	CF88_cpx 118_ap1	CF88_cpx 136_ap1	CF88_cpx 85_ap1	CF88_cpx 116_ap1	CF88_bt 36_ap1	CFmap1_C F25_41	CFmap1_C F25_29	CFmap1_C F25_19
Type:	mpc	mpc	cpx	cpx	cpx	cpx	bt	mpc	mpc	mpc
P ₂ O ₅	40.15	40.73	39.71	40.49	40.02	39.79	40.38	40.55	41.63	40.39
SiO ₂	0.72	0.45	1.50	1.33	1.25	1.28	1.08	0.77	0.42	0.66
CaO	54.23	54.03	52.48	52.90	53.55	52.78	53.70	53.02	54.27	53.43
SO ₂	0.72	0.41	0.00	0.00	0.56	0.00	0.53	0.36	0.37	0.68
F	2.69	2.02	2.79	2.88	2.48	2.84	2.72	2.18	2.14	2.14
Cl	0.61	0.89	0.42	0.43	0.63	0.41	0.54	1.15	0.94	1.10
OH	0.67	0.96	1.03	1.06	1.42	1.00	0.91	0.82	1.04	1.09
O = F, Cl, OH	1.59	1.50	1.76	1.81	1.86	1.76	1.69	1.56	1.60	1.66
Total	98.20	97.99	96.18	97.28	98.05	96.34	98.16	97.29	99.21	97.83
Eruption:	Pisani 1	Pisani 1	Pisani 1	Pisani 1	Pisani 1	Pisani 1	Pisani 1	Pisani 1	Pisani 1	Pisani 1
Crystal #:	CFmap1_C F25_7	CFmap1_C F25_44	CFmap1_C F25_5	CFmap1_C F25_2	CFmap1_C F25_22	CFmap1_C F25_30	CFmap1_C F25_18	CFmap1_C F25_46	CFmap1_C F25_37	CFmap1_C F25_50
Type:	mpc	mpc	mpc	mpc	mpc	mpc	mpc	mpc	mpc	mpc
P ₂ O ₅	41.14	42.19	39.38	41.82	38.27	38.17	40.64	41.45	42.14	41.11
SiO ₂	0.59	0.34	1.16	0.29	1.46	1.59	0.75	0.29	0.24	0.68
CaO	53.65	53.91	54.16	54.10	52.97	53.33	53.70	53.52	54.00	53.91
SO ₂	0.69	0.34	1.21	0.06	1.18	1.24	0.63	0.09	0.03	0.13
F	1.96	2.12	2.07	2.83	3.61	3.34	1.98	2.07	2.86	1.95
Cl	1.05	0.92	0.06	0.55	0.12	0.09	0.58	1.00	0.56	0.89
OH	0.95	0.99	1.39	0.35	0.33	0.40	1.21	0.76	0.32	0.96
O = F, Cl, OH	1.51	1.57	1.54	1.48	1.70	1.61	1.53	1.45	1.48	1.47
Total	98.52	99.24	97.89	98.52	96.24	96.55	97.96	97.73	98.67	98.16

(continued)

Table 3: Continued

Eruption: Crystal #:	Pisani 1 CFmap1_C F25_11	Pisani 1 CFmap1_C F25_9	Pisani 1 CFmap1_C F25_3	Pisani 1 CFmap1_C F25_1	Pisani 1 CFmap1_C F25_16	Pisani 1 CFmap1_C F25_27	Pisani 1 CFmap1_C F25_49	Pisani 1 CF25_cpx 98_ap2 cpx	Pisani 1 CF25_cpx 98_ap5 cpx	Pisani 1 CF25_cpx 121_ap1 cpx
Type:	mpc	mpc	mpc	mpc	mpc	mpc	mpc	mpc	mpc	mpc
P ₂ O ₅	39.29	39.66	40.88	42.41	42.02	42.09	41.94	40.79	40.22	40.04
SiO ₂	0.91	1.10	0.67	0.00	0.24	0.25	0.24	0.40	0.78	0.54
CaO	53.46	53.41	54.32	54.89	53.88	54.21	54.03	54.44	54.04	53.77
SO ₂	1.28	0.38	0.67	0.02	0.05	0.09	0.03	0.25	0.58	0.63
F	2.02	2.58	1.96	2.59	3.03	2.93	2.80	1.92	1.92	2.03
Cl	1.10	0.74	1.00	0.02	0.45	0.06	0.51	0.82	0.91	1.02
OH	0.90	0.69	0.93	0.99	0.28	0.44	0.48	1.01	1.01	1.04
O ≡ F, Cl, OH	1.52	1.58	1.49	1.56	1.51	1.45	1.52	1.47	1.49	1.58
Total	97.44	96.98	98.94	99.36	98.44	98.62	98.51	98.16	97.97	97.50
Eruption:	Pisani 1	Pisani 1	Pisani 1	Pisani 1	Pisani 1	Pisani 1	Pisani 1	Pomici Principali	Pomici Principali	Pomici Principali
Crystal #:	CF25_cpx 122_ap1 cpx	CF25_cpx 142_ap2 cpx	CF25_bt 40_ap1 bt	CF25_bt 67_ap2 bt	CF25_bt 98_ap1 bt	CF25_bt 112_ap1 bt	CF25_bt 110_ap1 bt	CFmap2_C F6_33 mpc	CFmap2_C F6_37 mpc	CFmap2_C F6_39 mpc
Type:	mpc	mpc	bt	bt	bt	bt	bt	mpc	mpc	mpc
P ₂ O ₅	40.88	40.68	41.56	40.36	41.27	39.20	41.47	40.86	38.06	41.25
SiO ₂	0.40	0.42	0.37	0.39	0.49	0.50	0.37	0.77	1.86	0.66
CaO	54.52	54.45	54.81	54.55	54.81	54.46	54.13	53.59	52.96	54.30
SO ₂	0.46	0.37	0.37	0.42	0.46	0.36	0.31	0.79	1.48	0.66
F	1.89	1.96	2.07	1.93	1.93	2.03	2.03	3.80	2.94	1.89
Cl	0.89	1.00	1.01	0.84	0.84	0.99	1.01	0.03	0.07	0.58
OH	1.10	0.81	0.93	1.20	0.97	1.04	0.90	0.24	1.21	1.97
O ≡ F, Cl, OH	1.52	1.44	1.54	1.57	1.46	1.57	1.50	1.72	1.82	1.85
Total	98.63	98.25	99.57	98.12	99.31	97.02	98.72	98.36	96.76	99.46
Eruption:	Pomici Principali	Pomici Principali	Pomici Principali	Pomici Principali	Pomici Principali	Pomici Principali	Pomici Principali	Pomici Principali	Pomici Principali	Pomici Principali
Crystal #:	CFmap2_C F6_47 mpc	CFmap2_C F6_25 mpc	CFmap2_C F6_24 mpc	CFmap2_C F6_30 mpc	CFmap2_C F6_32 mpc	CFmap2_C F6_16 mpc	CFmap2_C F6_10 mpc	CFmap2_C F6_13 mpc	CFmap2_C F6_6 mpc	CFmap2_C F6_5 mpc
Type:	mpc	mpc	mpc	mpc	mpc	mpc	mpc	mpc	mpc	mpc
P ₂ O ₅	41.61	41.66	41.79	42.03	40.00	40.46	41.71	41.03	42.00	42.06
SiO ₂	0.49	0.52	0.48	0.35	1.29	0.70	0.52	0.60	0.60	0.39
CaO	54.18	54.00	54.34	54.16	52.40	53.33	53.74	53.92	54.04	54.16
SO ₂	0.38	0.39	0.44	0.48	0.18	0.23	0.34	0.75	0.22	0.43
F	1.90	2.66	2.43	2.14	2.40	2.10	2.06	2.07	2.07	2.08
Cl	0.63	0.65	0.76	0.75	1.02	0.89	0.88	1.01	0.91	0.90
OH	1.50	0.91	1.01	1.31	1.16	1.09	1.12	1.12	1.15	1.14
O ≡ F, Cl, OH	1.65	1.69	1.67	1.69	1.79	1.60	1.59	1.63	1.62	1.62
Total	99.04	99.10	99.58	99.53	96.66	97.20	98.78	98.87	99.37	99.54
Eruption:	Pomici Principali	Pomici Principali	Pomici Principali	Pomici Principali	Pomici Principali	Pomici Principali	Pomici Principali	Pomici Principali	Pomici Principali	Pomici Principali
Crystal #:	CFmap2_C F6_46 mpc	CFmap2_C F6_21 mpc	CFmap2_C F6_100 mpc	CFmap2_C F6_15 mpc	CFmap2_C F6_26 mpc	CFmap2_C F6_98 mpc	CFmap2_C F6_92 mpc	CFmap2_C F6_62 mpc	CF6_cpx 19_ap1 cpx	CF6_cpx 64_ap1 cpx
Type:	mpc	mpc	mpc	mpc	mpc	mpc	mpc	mpc	mpc	mpc
P ₂ O ₅	41.36	42.04	39.99	41.04	41.45	40.93	40.23	40.05	41.35	40.50
SiO ₂	0.67	0.42	1.17	0.53	0.48	0.65	1.10	1.11	0.43	0.68
CaO	53.89	53.64	52.68	53.97	53.87	54.01	53.31	54.96	54.66	53.97
SO ₂	0.77	0.34	0.07	0.75	0.44	0.72	0.19	1.09	0.27	0.52
F	2.21	2.06	2.39	2.12	2.84	2.06	1.97	2.20	2.08	2.00
Cl	1.11	0.90	1.05	1.04	0.75	1.00	0.95	0.07	0.85	0.97
OH	0.95	1.02	0.85	0.88	0.19	0.89	0.99	1.30	0.93	1.35
O ≡ F, Cl, OH	1.63	1.55	1.64	1.54	1.45	1.51	1.51	1.55	1.51	1.70
Total	99.33	98.87	96.56	98.79	98.57	98.75	97.23	99.23	99.06	98.28
Eruption:	Pomici Principali	Pomici Principali	Pomici Principali	Pomici Principali	Pomici Principali	Minopoli 1	Minopoli 1	Minopoli 1	Minopoli 1	Minopoli 1
Crystal #:	CF6_cpx 96_ap1 cpx	CF6_cpx 138_ap1 cpx	CF6_bt 94_ap1 bt	CF6_bt 112_ap1 bt	CF6_bt 26_ap1 bt	CFmap1_C F13_39 mpc	CFmap1_C F13_50 mpc	CFmap1_C F13_15 mpc	CFmap1_C F13_16 mpc	CFmap1_C F13_3 mpc
Type:	mpc	mpc	bt	bt	bt	mpc	mpc	mpc	mpc	mpc
P ₂ O ₅	40.30	40.41	40.31	40.72	40.75	40.93	40.66	40.58	39.82	40.85
SiO ₂	0.70	0.96	0.93	0.68	0.76	0.60	0.48	0.89	0.75	0.37
CaO	53.58	53.94	53.39	54.16	54.04	54.34	54.54	53.57	53.63	54.34
SO ₂	0.51	0.64	0.60	0.51	0.55	0.63	0.18	0.81	0.81	0.36
F	2.14	1.94	2.26	2.22	2.27	2.16	3.11	2.27	1.94	2.03
Cl	0.93	0.90	0.95	0.97	0.97	0.55	0.03	0.74	0.63	1.08
OH	0.82	1.08	1.14	1.16	1.18	1.08	0.39	1.51	1.38	0.78
O ≡ F, Cl, OH	1.50	1.53	1.70	1.70	1.73	1.54	1.50	1.83	1.61	1.47
Total	97.47	98.34	97.87	98.72	98.80	98.75	97.89	98.54	97.35	98.34

(continued)

Table 3: Continued

Eruption: Crystal #:	Minopoli 1 CFmap1_C F13_4	Minopoli 1 CFmap1_C F13_7	Minopoli 1 CFmap1_C F13_22	Minopoli 1 CFmap1_C F13_31	Minopoli 1 CFmap1_C F13_27	Minopoli 1 CFmap1_C F13_2	Minopoli 1 CFmap1_C F13_10	Minopoli 1 CFmap1_C F13_42	Minopoli 1 CFmap1_C F13_19	Minopoli 1 CFmap1_C F13_8
Type:	mpc	mpc	mpc	mpc	mpc	mpc	mpc	mpc	mpc	mpc
P ₂ O ₅	39.50	40.81	40.04	41.03	40.78	40.13	40.70	41.37	41.39	42.39
SiO ₂	0.84	0.51	1.20	0.42	0.63	1.00	0.45	0.41	0.50	0.06
CaO	54.03	53.92	53.26	54.06	53.77	52.90	53.86	53.81	54.92	54.64
SO ₂	0.74	0.59	0.17	0.44	0.33	0.19	0.31	0.42	0.47	0.00
F	2.24	2.08	1.94	1.83	2.86	2.08	2.00	1.96	1.71	2.84
Cl	0.05	0.85	0.90	0.81	0.93	0.94	0.88	0.86	0.41	0.12
OH	1.35	1.01	1.10	0.98	0.24	1.04	0.97	0.88	1.29	0.51
O≡F, Cl, OH	1.59	1.54	1.54	1.41	1.53	1.58	1.50	1.43	1.42	1.46
Total	97.16	98.23	97.07	98.16	98.01	96.70	97.67	98.28	99.27	99.10

Eruption: Crystal #:	Minopoli 1 CFmap1_C F13_30	Minopoli 1 CFmap1_C F13_43	Minopoli 1 CFmap1_C F13_28	Minopoli 1 CFmap1_C F13_41	Minopoli 1 CFmap1_C F13_49	Minopoli 1 CFmap1_C F13_32	Minopoli 1 CF13_cpx 169_ap1 cpx	Minopoli 1 CF13_bt 114_ap1 bt	RP
Type:	mpc	mpc	mpc	mpc	mpc	mpc			
P ₂ O ₅	38.93	40.24	40.59	39.39	41.19	41.08	41.91	41.47	0.45
SiO ₂	1.34	0.60	0.58	1.20	0.39	0.53	0.42	0.55	0.05
CaO	54.05	54.82	53.61	54.10	53.81	54.51	54.40	54.15	0.50
SO ₂	1.36	0.44	0.74	0.97	0.11	0.44	0.41	0.55	0.03
F	2.45	3.24	2.32	1.81	2.02	2.12	1.94	1.94	0.18
Cl	0.06	0.02	0.56	0.48	0.70	0.88	0.76	0.83	0.15
OH	1.30	0.45	0.97	1.37	0.81	1.01	0.89	1.06	0.08
O≡F, Cl, OH	1.66	1.58	1.56	1.51	1.39	1.57	1.41	1.50	
Total	97.83	98.23	97.81	97.81	97.64	99.00	99.32	99.04	

Halogens and OH were measured by SIMS; all other elements were measured by EPMA. Crystal type refers to textural association: cpx, clinopyroxene-hosted inclusion; bt, biotite-hosted inclusion; mpc, microphenocryst. Concentrations are in wt %. RP is representative absolute precision with 1SD based on counting statistics for elements measured by EPMA, and a 95% confidence interval based on regression of calibration standards for elements measured by SIMS.

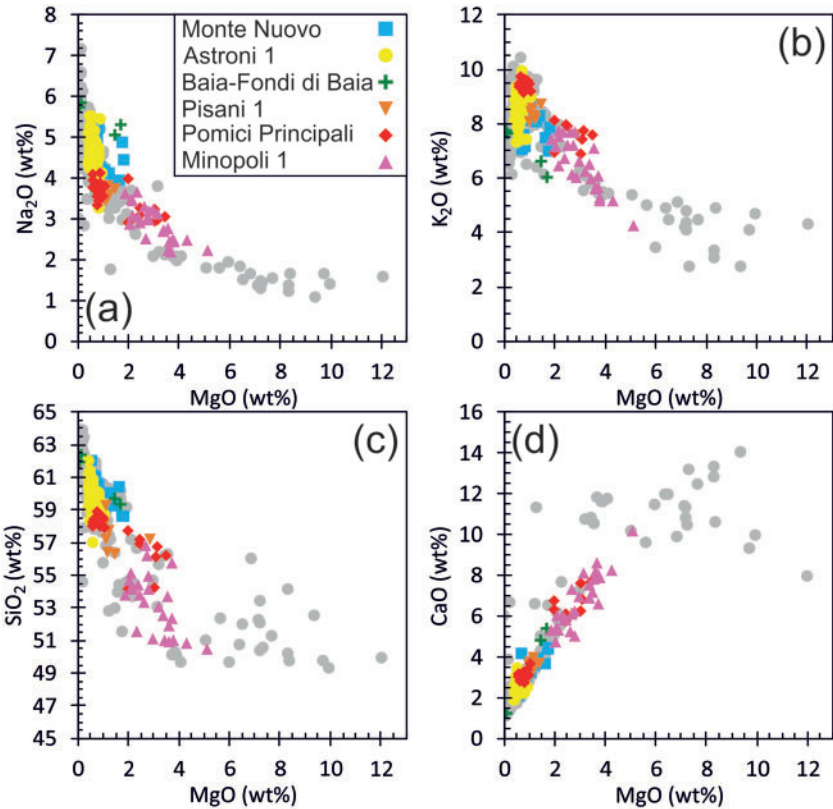


Fig. 2. Clinopyroxene-hosted melt inclusion major element compositions from explosive Campi Flegrei eruptions. All data were measured by EPMA and are normalized to 100%. Data are distinguished by eruption (see legend). Grey points show a compilation of literature clinopyroxene- and olivine-hosted melt inclusion compositions in <15 ka Campi Flegrei deposits from Cannatelli *et al.* (2007), Mangiacapra *et al.* (2008), Arienzo *et al.* (2010, 2016) and Fourmentraux *et al.* (2012).

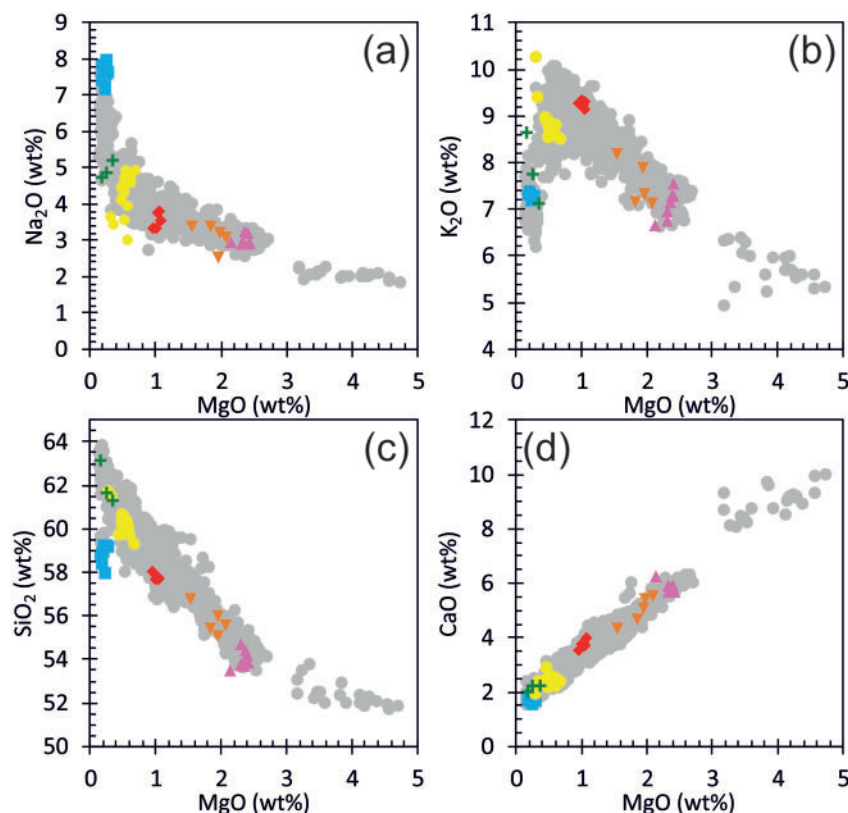


Fig. 3. Matrix glass major element compositions from explosive Campi Flegrei eruptions. All data were measured by EPMA and are normalized to 100%. Data are distinguished by eruption (see legend in Fig. 2). Grey points are literature matrix glass compositions in <15 ka Campi Flegrei deposits from Smith *et al.* (2011).

depleted and Na₂O-rich (Fig. 3). This is consistent with fractional crystallization models, which indicate early fractionation of olivine, clinopyroxene and magnetite (Fowler *et al.*, 2007) but show a major change in compatibility for K₂O and Na₂O at ~0.5 wt % MgO, after plagioclase, biotite and K-feldspar come onto the liquidus (Fowler *et al.*, 2007; Cannatelli, 2012; Stock *et al.*, 2016).

Glass volatile compositions

Campi Flegrei melt inclusions analysed in this study show that Cl generally increases as MgO decreases, consistent with previous analyses (Fig. 4a). Minopoli 1 melt inclusions have the lowest Cl concentrations (0.32–0.85 wt %), whereas melt inclusions from Pisani 1 and PP are intermediate (0.58–0.89 wt %). Melt inclusions from other eruptions have higher Cl concentrations, extending up to 1.17 wt % (Fig. 4a; Supplementary Data Table S1). Matrix glass Cl contents are typically similar to melt inclusions; the most Cl-depleted matrix glasses (0.50–0.79 wt %) are from Minopoli 1 and Pisani 1, with the highest Cl concentrations in matrix glasses from Monte Nuovo and B-FdB reaching 1.20 wt % (Fig. 4b; Supplementary Data Table S1). Some low-MgO (<0.5 wt %) matrix glasses from Astroni 1 and B-FdB have low Cl contents (<0.6 wt %), in agreement with the greater variability in matrix glass Cl concentrations at low MgO previously reported in the literature (Fig. 4b).

Mafic (≥ 2 wt % MgO) melt inclusions from Campi Flegrei show scattered F contents, with concentrations up to 0.46 wt % F in Minopoli 1 (Fig. 4c). In more evolved melt inclusions (≤ 2 wt % MgO), F is typically higher in inclusions with lower MgO contents, from <0.1 wt % in Pisani 1 and PP to ~0.4 wt % in B-FdB (Fig. 4c; Supplementary Data Table S1). Fluorine concentrations up to 0.61 wt % have been reported in very low MgO melt inclusions (Fourmentaux *et al.*, 2012). In general, matrix glass F concentrations are approximately constant (~0.1–0.3 wt %; Fig. 4d). However, F is significantly enriched in low-MgO (<0.5 wt %) matrix glasses from Monte Nuovo (typically 0.6–0.8 wt % F), with a single analysis reaching 1.26 wt %.

Melt inclusions analysed in this study typically contain ~2–4 wt % H₂O and show no correlation between H₂O and MgO (Fig. 4e), consistent with other Campi Flegrei eruptions (Arienzo *et al.*, 2016). Some inclusions have H₂O concentrations as low as 1.04 wt %, with the largest variability at low MgO concentrations (<1.5 wt %), where measured H₂O concentrations extend to >5 wt %, within the range previously reported for <15 kyr Campi Flegrei eruptions (up to 6.96 wt %; Cannatelli *et al.*, 2007). Matrix glass H₂O contents are lower than in melt inclusions; mafic Minopoli 1 and Pisani 1 matrix glasses consistently have H₂O concentrations <0.4 wt %, whereas more evolved (<1 wt % MgO) PP, Astroni 1 and Monte Nuovo matrix glasses

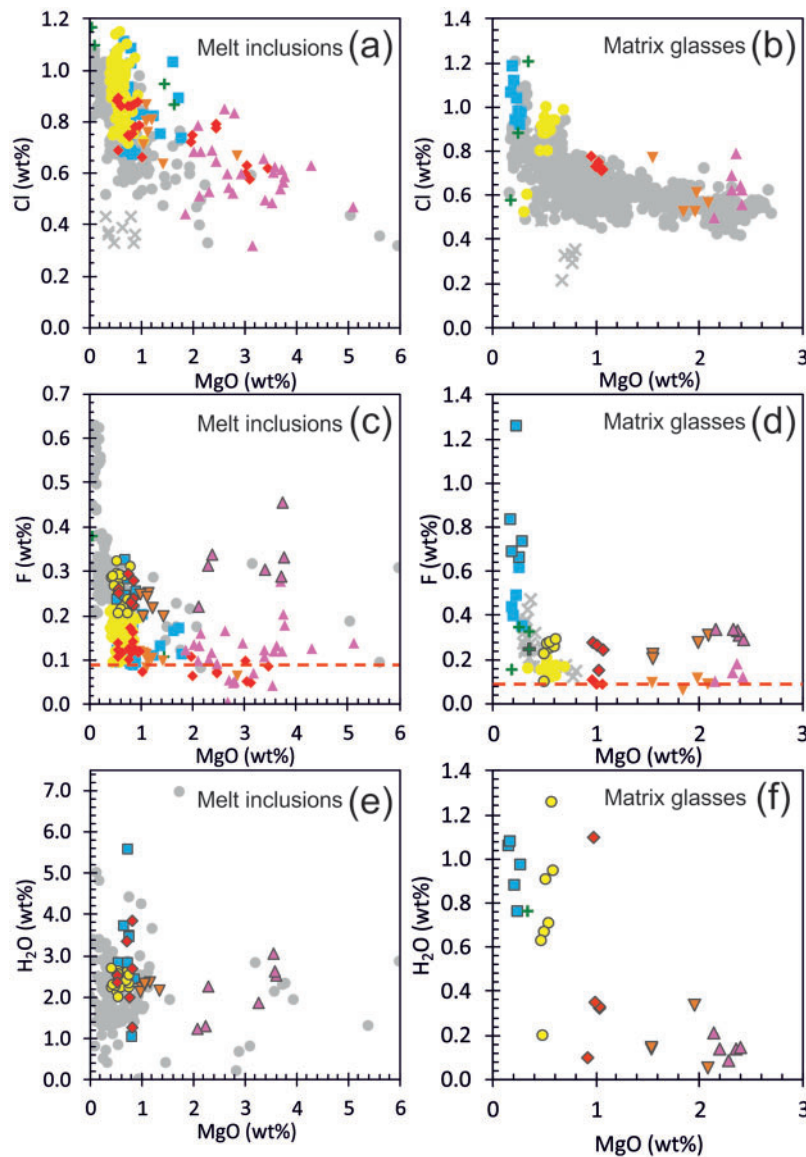


Fig. 4. Halogens (a–d) and H_2O (e, f) vs MgO compositions of melt inclusions (a, c, e) and matrix glasses (b, d, f) from explosive Campi Flegrei eruptions. MgO and Cl were measured by EPMA, H_2O was measured by SIMS, and F was measured by EPMA (points with no outlines) and SIMS (points with grey outlines). The red dashed lines show EPMA F detection limits of 0.09 wt %. Data in (a)–(d) are normalized to 100%. Data are distinguished by eruption (see legend in Fig. 2). Grey circles show literature melt inclusion and matrix glass compositions in <15 ka Campi Flegrei deposits, from the same sources as Figs 2 and 3, respectively. The grey crosses show the compositions of Campanian Ignimbrite melt inclusions and matrix glasses from Signorelli *et al.* (1999).

have more variable H_2O concentrations, extending to >1 wt % (Fig. 4f).

Apatite volatile compositions

Apatite inclusions

Clinopyroxene-hosted apatite inclusions have measured F concentrations from 1.86 to 2.92 wt %, Cl concentrations from 0.41 to 1.27 wt % and OH concentrations from 0.39 to 1.42 wt % (Table 3; Supplementary Data Table S2). This translates to $X_{\text{Cl}}/X_{\text{OH}}$ ratios from 0.19 to 1.22, $X_{\text{F}}/X_{\text{OH}}$ from 1.33 to 5.79 and $X_{\text{F}}/X_{\text{Cl}}$ from 2.96 to 12.8 (where X_{F} , X_{Cl} and X_{OH} are the mole fractions of F, Cl and OH, respectively). Variations in the apatite volatile site can typically be described by an F–OH

exchange, with an approximately constant Cl component (Fig. 5a). Baia–Fondi di Baia is an exception, where Cl in clinopyroxene-hosted apatite inclusions is notably depleted relative to inclusions in other eruptions. In general, clinopyroxene-hosted apatite inclusions show a positive correlation between $X_{\text{Cl}}/X_{\text{OH}}$ and $X_{\text{F}}/X_{\text{OH}}$ and approximately constant $X_{\text{F}}/X_{\text{Cl}}$ (Fig. 5b and c).

Biotite-hosted apatite inclusions have a more restricted compositional range than clinopyroxene-hosted inclusions, with F, Cl and OH ranging from 1.81 to 2.76 wt %, 0.54 to 1.17 wt % and 0.53 to 1.20 wt %, respectively (Table 3; Supplementary Data Table S2). This translates to $X_{\text{Cl}}/X_{\text{OH}}$ ratios from 0.28 to 0.95, $X_{\text{F}}/X_{\text{OH}}$ from 1.20 to 4.11 and $X_{\text{F}}/X_{\text{Cl}}$ from 3.31 to 9.47. Biotite-

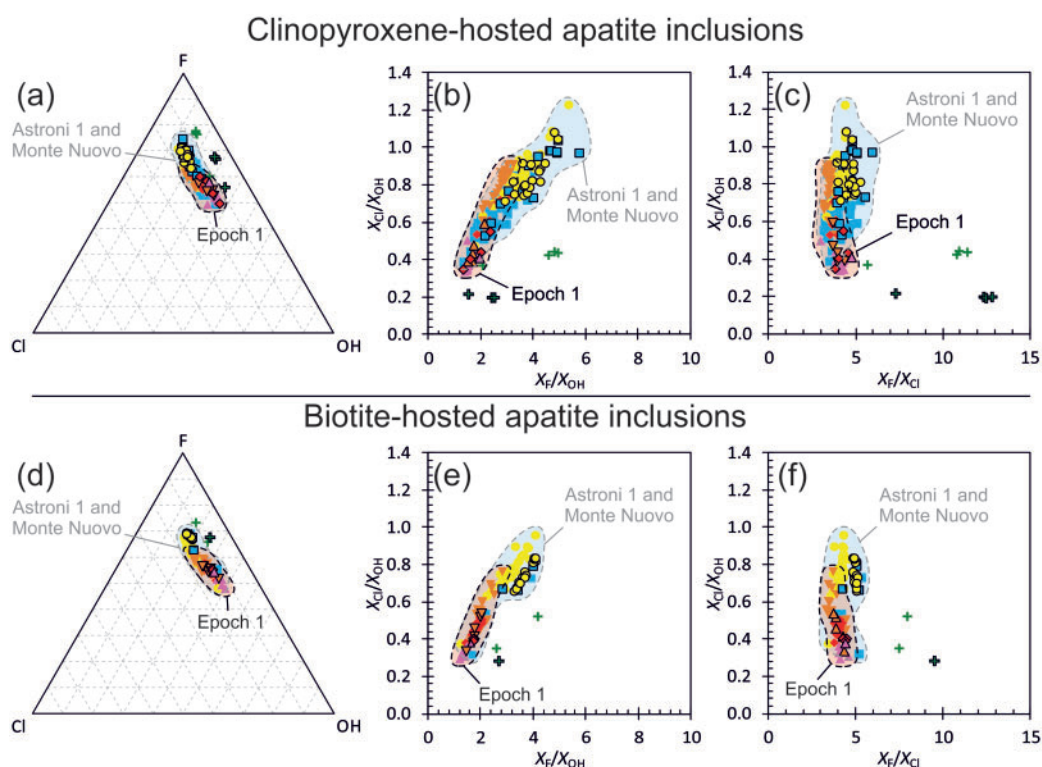


Fig. 5. Volatile compositions of clinopyroxene- (a–c) and biotite-hosted (d–f) apatite inclusions from explosive Campi Flegrei eruptions. Data are presented both in ternary space (a, d) and on binary plots of $X_{\text{Cl}}/X_{\text{OH}}$ vs $X_{\text{F}}/X_{\text{OH}}$ (b, e) and $X_{\text{Cl}}/X_{\text{OH}}$ vs $X_{\text{F}}/X_{\text{Cl}}$ (c, f). Points with black outlines were measured by SIMS and points without outlines were measured by EPMA. Data are distinguished by eruption (see legend in Fig. 2). The coloured fields highlight EPMA and SIMS data from Epoch 1 (red), and Astroni 1 (Epoch 3) and the historical Monte Nuovo eruptions (blue).

hosted inclusions plot on the same compositional trends as clinopyroxene-hosted inclusions (Fig. 5d–f). However, within an individual eruption, biotite-hosted inclusions are typically offset to more OH-rich compositions, with lower $X_{\text{Cl}}/X_{\text{OH}}$ and $X_{\text{F}}/X_{\text{OH}}$ ratios (Table 3; Supplementary Data Table S2).

Apatite microphenocrysts

Apatite microphenocrysts show more compositional diversity than inclusions (Figs 5–7), with a small minority of F concentrations measured by EPMA reaching 4.54 wt %. These high F contents are almost exclusively in lava samples (Supplementary Data Table S2) but exceed the maximum stoichiometric limit of 3.76 wt % F (Pyle *et al.*, 2002), probably reflecting electron beam-induced sample damage in near end-member fluorapatite (Stormer *et al.*, 1993; Goldoff *et al.*, 2012; Stock *et al.*, 2015). The highest F concentrations measured by SIMS (3.80 wt %; Table 3) are stoichiometric within analytical uncertainty. In apatite microphenocrysts, the minimum F concentration is 1.67 wt %, Cl ranges from 0.02 to 1.47 wt % and measured OH concentrations are <1.97 wt % (Table 3; Supplementary Data Table S2). This translates to overall $X_{\text{Cl}}/X_{\text{OH}}$, $X_{\text{F}}/X_{\text{OH}}$ and $X_{\text{F}}/X_{\text{Cl}}$ ratios from ~0 to 16.5, 0.86 to 781 and 2.85 to 374, respectively, with $X_{\text{Cl}}/X_{\text{OH}} \leq 2.27$ and $X_{\text{F}}/X_{\text{OH}} \leq 25.8$ in explosive eruptions. Most apatite microphenocrysts

plot on the same compositional trends as the inclusions (Figs 6 and 7) but typically extend to more OH-rich compositions with lower $X_{\text{Cl}}/X_{\text{OH}}$ and $X_{\text{F}}/X_{\text{OH}}$ ratios. Compositional differences between apatite inclusions and microphenocrysts along this main trend were used by Stock *et al.* (2016) to give temporal context to apatite data from Astroni 1. Two subsidiary sets of apatite microphenocrysts are observed in some explosive eruptions, both with lower Cl contents than the main trend (Figs 6 and 7). One has low $X_{\text{Cl}}/X_{\text{OH}}$ ratios with $X_{\text{F}}/X_{\text{OH}}$ and $X_{\text{F}}/X_{\text{Cl}}$ ratios that extend to very high values (i.e. in Monte Nuovo, Astroni 1, B-FdB, Pisani 1, PP, Minopoli 1); the other has high $X_{\text{Cl}}/X_{\text{OH}}$ and $X_{\text{F}}/X_{\text{OH}}$ ratios (i.e. in Astroni 1, B-FdB, PP, Minopoli 1). Additionally, a small number of inclusions from Pisani 1 define a trend towards high $X_{\text{F}}/X_{\text{OH}}$ at similar $X_{\text{Cl}}/X_{\text{OH}}$ ratios to the main population (Fig. 7d–f). Apatite microphenocrysts from lava deposits (Accademia and SMdG) are distinct; in ternary space they typically show an increasing F component at the expense of Cl, trending first towards the F–Cl join and then curving towards the F apex, but in binary space they are scattered with no discernible trend (Fig. 6g–i).

Differences between eruptions

The SIMS analyses are more precise than the EPMA data, so subtle differences in apatite compositions

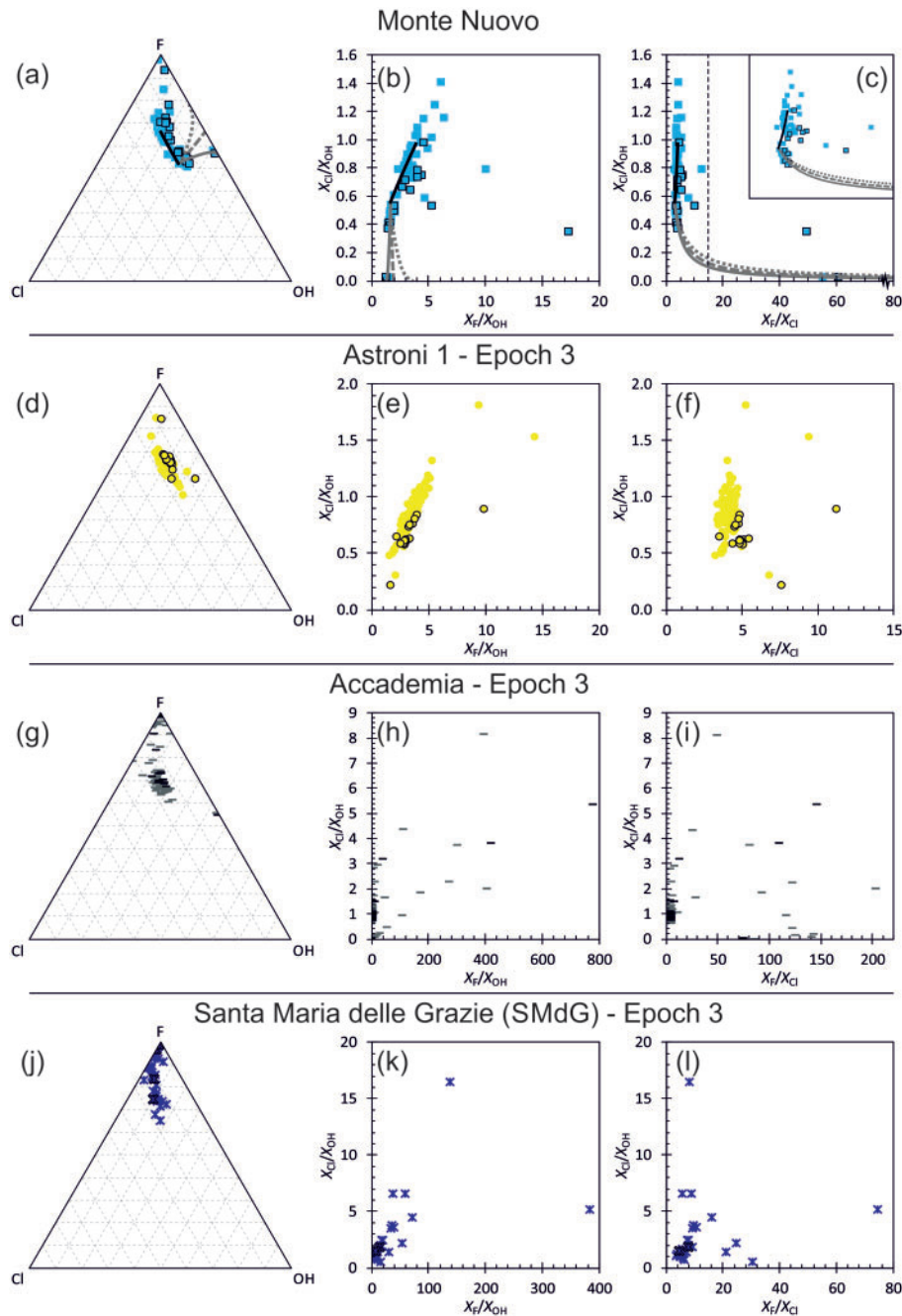


Fig. 6. Volatile compositions of apatite microphenocrysts from the historical Monte Nuovo (a–c) and Epoch 3 (d–l) eruptions of Campi Flegrei. Data are presented both in ternary space (a, d, g, j) and on binary plots of $X_{\text{Cl}}/X_{\text{OH}}$ vs $X_{\text{F}}/X_{\text{OH}}$ (b, e, h, k) and $X_{\text{Cl}}/X_{\text{OH}}$ vs $X_{\text{F}}/X_{\text{Cl}}$ (c, f, i, l). Inset in (c) shows an expansion of the area outlined by the black dashed box in the main panel. Points with black outlines were measured by SIMS and points without outlines were measured by EPMA. Non-stoichiometric analyses with F > 3.76 wt % (i.e. in lava deposits) are plotted as end-member fluorapatite, with non-stoichiometry probably the result of F migration during EPMA (Stormer *et al.*, 1993; Goldoff *et al.*, 2012; Stock *et al.*, 2015). Data are distinguished by eruption (see headings). Lines in (a)–(c) show the theoretical trajectory of apatite compositional evolution predicted by our thermodynamic model that best fits natural apatite compositions from Campi Flegrei. $C_{\text{Cl}}^0 = 0.4$ wt %, $C_{\text{F}}^0 = 0.2$ wt %, $C_{\text{H}_2\text{O}}^0 = 2.5$ wt %, $K_{\text{Cl-F}}^{\text{ap-m}} = 0.22$, $K_{\text{Cl-OH}}^{\text{ap-m}} = 25$, $K_{\text{F-OH}}^{\text{ap-m}} = 75$, $\bar{D}_{\text{F}}^{\text{c/m}} = 0.99$, $\bar{D}_{\text{Cl}}^{\text{c/m}} = 0.8$, and $\bar{D}_{\text{H}_2\text{O}}^{\text{c/m}} = 0.01$. H_2O speciation is calculated after Zhang (1999) for a temperature of 1020°C. The black continuous line shows modelled apatite compositional evolution during ~70% volatile-undersaturated crystallization. The grey lines show modelled apatite compositional evolution during subsequent H_2O -saturated crystallization, with $D_{\text{Cl}}^{\text{f/m}} = 20$ and $D_{\text{F}}^{\text{f/m}} = 0.7$, after $C_{\text{H}_2\text{O}}^{\text{m}}$ reaches $C_{\text{H}_2\text{O}}^{\text{sat}}$ at 7.5 wt %. The grey line types illustrate the difference between isobaric (0% H_2O loss; continuous lines) H_2O -saturated crystallization and polybaric H_2O -saturated crystallization with 0.15 wt % (dashed lines) and 0.25 wt % (dotted lines) H_2O loss from the melt into the fluid phase per 1% crystallization.

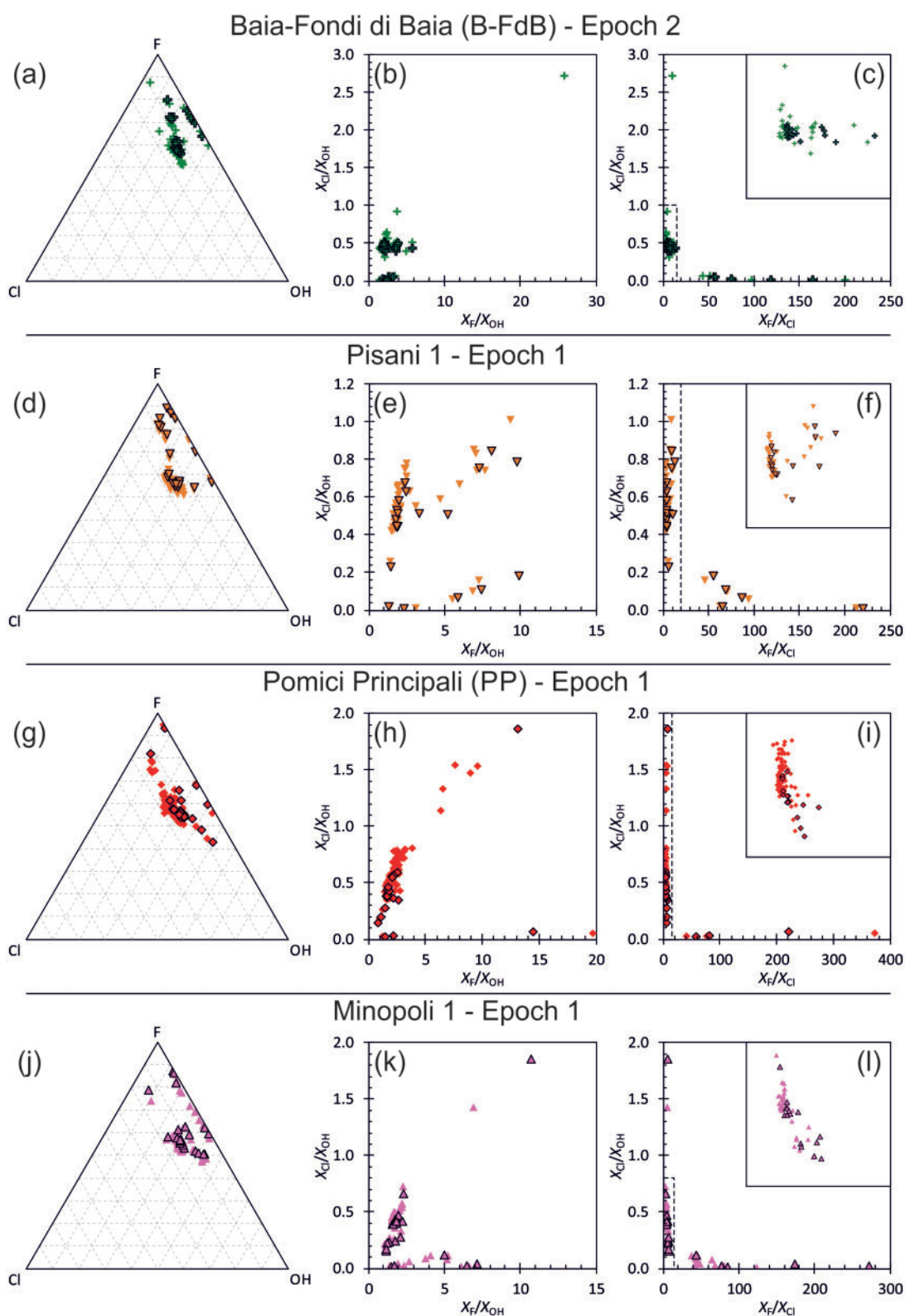


Fig. 7. Volatile compositions of apatite microphenocrysts from Epoch 2 (Baia-Fondi di Baia; a–c) and Epoch 1 (d–l) Campi Flegrei eruptions. Data are presented both in ternary space (a, d, g, j) and on binary plots of X_{Cl}/X_{OH} vs X_F/X_{OH} (b, e, h, k) and X_{Cl}/X_{OH} vs X_F/X_{Cl} (c, f, i, l). Insets in (c), (f), (i) and (l) show expansions of the areas outlined by the black dashed boxes in the main panels. Points with black outlines were measured by SIMS and points without outlines were measured by EPMA. Data are distinguished by eruption (see headings).

between eruptions are more clearly resolved. Clinopyroxene- and biotite-hosted apatite inclusions from Epoch 1 eruptions (Minopoli 1, PP and Pisani 1) are typically more OH-rich than those from the more recent Astroni 1 (Epoch 3) and Monte Nuovo eruptions; this translates to lower $X_{\text{Cl}}/X_{\text{OH}}$ and $X_{\text{F}}/X_{\text{OH}}$ and slightly lower $X_{\text{F}}/X_{\text{Cl}}$ ratios in apatite inclusions from Epoch 1 than in those from younger eruptions (Fig. 5). The main population of apatite microphenocrysts from Astroni 1 is also typically more F-rich, with higher $X_{\text{Cl}}/X_{\text{OH}}$, $X_{\text{F}}/X_{\text{OH}}$ and $X_{\text{F}}/X_{\text{Cl}}$ ratios than those from Epoch 1 eruptions. Monte Nuovo microphenocrysts in this population extend to higher $X_{\text{Cl}}/X_{\text{OH}}$, $X_{\text{F}}/X_{\text{OH}}$ and $X_{\text{F}}/X_{\text{Cl}}$ ratios than those from Epoch 1, but cover the entire compositional diversity of the main microphenocryst population from other eruptions (Figs 6 and 7). Baia-Fondi di Baia inclusions (Epoch 2) are relatively $X_{\text{Cl}}/X_{\text{OH}}$ depleted; B-FdB microphenocrysts are compositionally similar to those of Epoch 1 (i.e. comparable $X_{\text{Cl}}/X_{\text{OH}}$) but follow a different evolutionary trajectory. There is more overlap between eruptions in the lower-precision EPMA dataset but it is still clear that apatite inclusions and microphenocrysts from younger eruptions (Astroni 1 and Monte Nuovo) extend to more F-rich compositions, with higher $X_{\text{Cl}}/X_{\text{OH}}$, $X_{\text{F}}/X_{\text{OH}}$ and $X_{\text{F}}/X_{\text{Cl}}$ ratios, than those from Epoch 1 (Figs 5–7).

THERMODYNAMIC FRAMEWORK FOR APATITE VOLATILE INTERPRETATION

The composition of the apatite volatile site is described by a series of exchange equilibria between F, Cl and OH (e.g. Pan & Fleet, 2002); for example,



where X denotes mole fraction in the apatite (Ap) and melt (m) phases. Exchange coefficients (K) for these equilibria are defined as

$$K_{\text{Cl-OH}(P,T)}^{\text{Ap/m}} = \frac{a_{\text{Cl}}^{\text{Ap}}}{a_{\text{OH}}^{\text{Ap}}} \cdot \frac{a_{\text{OH}}^{\text{m}}}{a_{\text{Cl}}^{\text{m}}} \quad (2)$$

where a is activity. The evolution of F, Cl and H_2O concentrations in the melt (i.e. a_{OH}^{m} and so on) during fractional crystallization depends on the nature of both crystal–melt partitioning and fluid–melt exchange. Therefore, we can predict how apatite compositions in equilibrium with the melt will evolve during different fractional crystallization scenarios using appropriate experimental K_{D} values from the literature.

We have developed a thermodynamic model, relating apatite compositional evolution to changes in the volatile contents of silicate melts during crystallization in the presence or absence of different magmatic fluids, building on the work of Candela (1986), who treated halogens and H_2O as perfectly incompatible during volatile-undersaturated crystallization. First, we

calculate the evolution of F, Cl and H_2O in the melt owing to crystal \pm fluid fractionation. We then compute the volatile composition of apatite in equilibrium with the melt at each stage of the crystallization model. We assume that the apatite solid solution is ideal and that the apatite–melt exchange coefficients are unaffected by the changing melt composition. The validity of these assumptions, definitions of terminology, and the values of key parameters, including mineral–melt and fluid–melt partition coefficients and the solubility of halogens and H_2O in the silicate melt, are discussed in the [Supplementary Data](#). Our approach can be applied generally to determine apatite compositions during fractional crystallization. The effects of pressure and temperature variations on apatite compositions are also outlined below.

Apatite fractional crystallization models

The initial melt Cl (C_{Cl}^0) and F (C_{F}^0) concentrations are set at 0.4 wt % and 0.2 wt %, respectively, based on the mafic melt inclusion compositions given in [Table 2](#) and [Supplementary Data Table S1](#). The initial melt H_2O concentration ($C_{\text{H}_2\text{O}}^0$) is set at 2.5 wt %, similar to the predicted Campi Flegrei melt H_2O concentration at *apatite-in* from Rhyolite-MELTS (Stock *et al.*, 2016) and initial H_2O concentrations used for modelling by Fowler *et al.* (2007) and Cannatelli (2012).

During volatile-undersaturated crystallization, the evolution of all volatile components in the melt is described by the Rayleigh equation:

$$C_i^{\text{m}} = C_i^0 \cdot \varphi^{\bar{D}_i^{\text{c/m}} - 1} \quad (3)$$

where C_i^{m} is the concentration of i in the melt at a given melt fraction (φ) and $\bar{D}_i^{\text{c/m}}$ is the bulk crystal–melt partition coefficient.

We simulate the onset of saturation with an H_2O -rich fluid by imposing a pre-defined H_2O solubility limit ($C_{\text{H}_2\text{O}}^{\text{sat}}$), here taken as 7.5 wt % H_2O , which is appropriate for phonolite liquids at 200 MPa (Webster *et al.*, 2014). Once this solubility limit is reached, the H_2O concentration in the melt is held constant to simulate isobaric fractionation (or can be linearly decreased to illustrate the effect of polybaric decompression). Further H_2O that exsolves owing to continuing fractionation is assigned to a separate fluid phase, following Candela & Holland (1986), and we calculate the F and Cl concentration of that fluid phase using the fluid–melt partition coefficients (i.e. $D_{\text{F}}^{\text{f/m}}$ and $D_{\text{Cl}}^{\text{f/m}}$, respectively). This fluid is iteratively extracted from the evolving melt by mass balance. We calculate mole fractions of Cl, F and total H_2O in the melt following Li & Hermann (2017) and use the H_2O speciation model of Zhang (1999) for a temperature of 1020°C to calculate the mole fraction of OH in the melt. Finally, we calculate the mole fraction of F-apatite, Cl-apatite and OH-apatite in equilibrium with the calculated melt composition, following Candela (1986), and thus apatite $X_{\text{Cl}}/X_{\text{OH}}$, $X_{\text{F}}/X_{\text{OH}}$ and $X_{\text{F}}/X_{\text{Cl}}$.

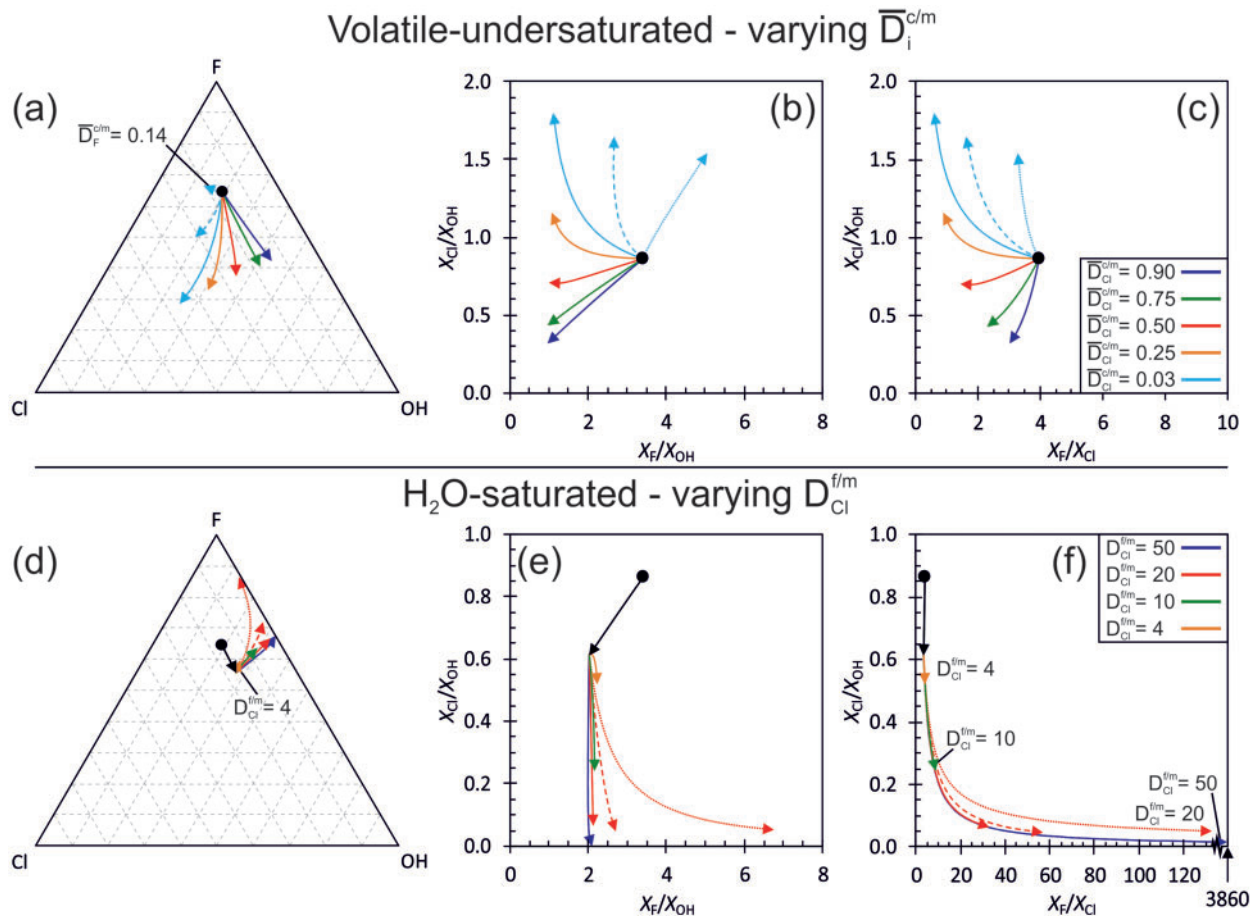


Fig. 8. Theoretical apatite compositional trajectories for different crystallization scenarios (not specific to Campi Flegrei). Data are presented both in ternary (a, d) space and on binary plots of $X_{\text{Cl}}/X_{\text{OH}}$ vs $X_{\text{F}}/X_{\text{OH}}$ (b, e) and $X_{\text{Cl}}/X_{\text{OH}}$ vs $X_{\text{F}}/X_{\text{Cl}}$ (c, f). In all models, $C_{\text{Cl}}^0 = 0.4$ wt %, $C_{\text{F}}^0 = 0.2$ wt %, $C_{\text{H}_2\text{O}}^0 = 2.9$ wt %, $K_{\text{Cl-F}}^{\text{ap-m}} = 0.22$, $K_{\text{Cl-OH}}^{\text{ap-m}} = 25$, $K_{\text{F-OH}}^{\text{ap-m}} = 75$, and apatite crystallization begins at the black point (see discussion of input parameters in the text). H_2O speciation is calculated after Zhang (1999) for a temperature of 1020°C . (a–c) Apatite compositional evolution during volatile-undersaturated fractional crystallization. Crystal compositions evolve in the arrow direction until 85% crystallization. Curves show the effect of varying $\bar{D}_1^{\text{c/m}}$, where $\bar{D}_{\text{F}}^{\text{c/m}} > \bar{D}_{\text{Cl}}^{\text{c/m}} > \bar{D}_{\text{H}_2\text{O}}^{\text{c/m}}$ and $1 > \bar{D}_1^{\text{c/m}} > 0$. Line colours distinguish models with different $\bar{D}_{\text{Cl}}^{\text{c/m}}$ values [see legend in (c)]. Line types distinguish models with $\bar{D}_{\text{F}}^{\text{c/m}} = 0.99$ (continuous lines), $\bar{D}_{\text{F}}^{\text{c/m}} = 0.5$ (dashed lines) and $\bar{D}_{\text{F}}^{\text{c/m}} = 0.14$ (dotted lines). $\bar{D}_{\text{H}_2\text{O}}^{\text{c/m}}$ is set at 0.003; varying $\bar{D}_{\text{F}}^{\text{c/m}}$ affects crystal $X_{\text{F}}/X_{\text{OH}}$ and $X_{\text{Cl}}/X_{\text{OH}}$ evolution in the opposing sense to $\bar{D}_{\text{F}}^{\text{c/m}}$ and $\bar{D}_{\text{Cl}}^{\text{c/m}}$. (d–f) Apatite compositional evolution during H_2O -saturated fractional crystallization. The black arrow shows an arbitrary trajectory of apatite compositional evolution under volatile-undersaturated conditions ($\bar{D}_{\text{F}}^{\text{c/m}} = 0.8$, $\bar{D}_{\text{Cl}}^{\text{c/m}} = 0.65$, $\bar{D}_{\text{H}_2\text{O}}^{\text{c/m}} = 0.001$), until 61% crystallization. Water saturates at 61% crystallization when $C_{\text{H}_2\text{O}}^{\text{m}} = C_{\text{H}_2\text{O}}^{\text{sat}} = 7.5$ wt % (see Supplementary Data) and crystal compositions continue to evolve in the arrow direction to 85% crystallization. Line colours distinguish H_2O -saturated models with varying $\bar{D}_{\text{Cl}}^{\text{f/m}}$ within a realistic range [see legend in (f)]. $\bar{D}_{\text{Cl}}^{\text{f/m}} = 4$ equates to the lowest value measured for phonolitic systems at 150 MPa by Signorelli & Carroll (2000) and apatite trajectories at $\bar{D}_{\text{Cl}}^{\text{f/m}} > 50$ are almost indistinguishable. $\bar{D}_{\text{F}}^{\text{f/m}} = 0.7$ in all models (see Supplementary Data) and $\bar{D}_{\text{H}_2\text{O}}^{\text{f/m}}$ values are unaltered after H_2O -saturation. If fluid–melt Cl partitioning is non-Nernstian (Supplementary Data), apatite compositional evolution will not follow any single trajectory at set $\bar{D}_{\text{Cl}}^{\text{f/m}}$ but will cross between these lines towards higher $\bar{D}_{\text{Cl}}^{\text{f/m}}$. Line types illustrate the difference between isobaric (0% H_2O loss; continuous lines) H_2O -saturated crystallization and polybaric H_2O -saturated crystallization with 0.1 wt % (dashed lines) and 0.25 wt % (dotted lines) H_2O loss per 1% crystallization.

Model outputs: apatite compositional evolution during fractional crystallization

During volatile-undersaturated crystallization for a range of parameters (see Supplementary Data), apatite compositions typically show a decrease in both $X_{\text{F}}/X_{\text{OH}}$ and $X_{\text{F}}/X_{\text{Cl}}$ ratios, whereas $X_{\text{Cl}}/X_{\text{OH}}$ may increase or decrease depending on the exact values of the crystal–melt partition coefficients for F, Cl and OH (Fig. 8b and c). In contrast, H_2O -saturated crystallization is

characterized by a strong decrease in apatite $X_{\text{Cl}}/X_{\text{OH}}$ ratios per unit crystallization, with increasing $X_{\text{F}}/X_{\text{Cl}}$ and variable $X_{\text{F}}/X_{\text{OH}}$ (Fig. 8e and f). This is because fluid–melt partition coefficients for Cl are typically much higher than for F (Borodulin *et al.*, 2009; Webster *et al.*, 2014). In ternary space, volatile-undersaturated trajectories are typified by apatite compositional evolution away from the F apex (Fig. 8a). Conversely, during H_2O -saturated crystallization apatite compositions move

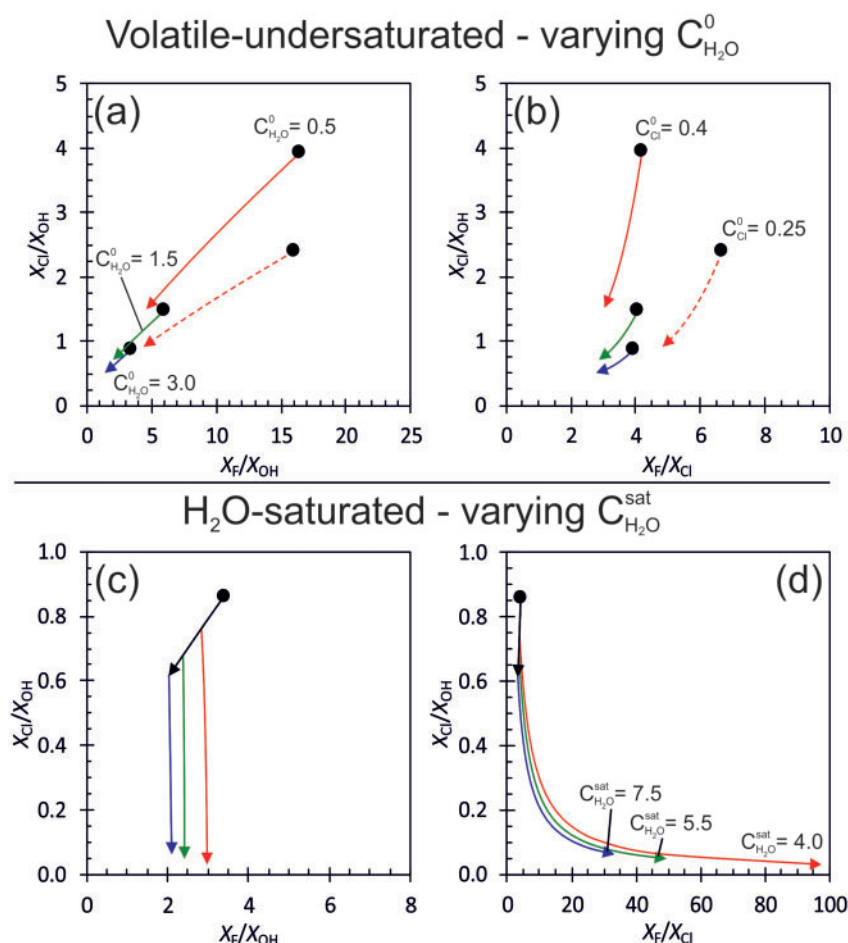


Fig. 9. The effect of varying input parameters in general (i.e. not specific to Campi Flegrei) thermodynamic models of apatite compositional evolution in X_{Cl}/X_{OH} vs X_F/X_{OH} (a, c) and X_{Cl}/X_{OH} vs X_F/X_{Cl} (b, d) binary space. C_F^0 , $D_F^{c/m}$, $D_{Cl}^{c/m}$, $D_{H_2O}^{c/m}$, $D_F^{f/m}$, K_{F-OH}^{ap-m} , K_{Cl-OH}^{ap-m} , K_{F-OH}^{ap-m} and H_2O speciation are as in Fig. 8d–f. Apatite crystallization begins at the black point and continues to 85% crystallization in all models. (a, b) Trajectories of volatile-undersaturated apatite compositional evolution with varying C_i^0 . Line colours distinguish models with $C_{H_2O}^0 = 3.0$ wt % (purple), $C_{H_2O}^0 = 1.5$ wt % (green) and $C_{H_2O}^0 = 0.5$ wt % (red). Line types distinguish models with $C_{Cl}^0 = 0.4$ wt % (continuous lines) and $C_{Cl}^0 = 0.25$ wt % (dashed lines). (c, d) Trajectories of apatite compositional evolution with varying $C_{H_2O}^{sat}$. C_{Cl}^0 and $C_{H_2O}^0$ are as in Fig. 8 and $D_{Cl}^{f/m} = 20$. The black arrows show an arbitrary trajectory of 61% volatile-undersaturated crystallization, as in Fig. 8e and f. Line colours show isobaric (0% H_2O loss) H_2O -saturated crystallization after 61%, 47% and 28% crystallization, where $C_{H_2O}^{sat}$ is 7.5 wt % (purple), 5.5 wt % (green) and 4 wt % (red), respectively.

towards the F–OH binary (Fig. 8d). Under polybaric H_2O -saturated conditions, where H_2O is lost from the melt during depressurization, crystal compositions may then curve towards the F apex (Fig. 8d).

The melt volatile composition

Varying the initial melt volatile concentrations (C_i^0) translates the starting point of the model in apatite compositional space, and changes the relative magnitudes of the calculated variations in apatite volatile components per unit crystallization. However, the slope or direction in binary or ternary space remains the same (Fig. 9a and b). In the general H_2O -saturated case, decreasing $C_{H_2O}^{sat}$ (e.g. at lower pressure or a different melt composition) reduces the extent of volatile-undersaturated crystallization before second boiling, but does not affect the trajectory of apatite compositional evolution after volatile-

saturation is achieved (Fig. 9c and d). Our model does not deal with saturation of either fluorite, which is present only as a late-stage accessory mineral, or brine. Fluorine and Cl act as incompatible elements during fractionation (i.e. higher halogen concentrations in low-MgO in glass analyses; Fig. 4a–d), which suggests that brine exsolution is also not a major factor at Campi Flegrei. We would anticipate that formation of fluorite and/or brine would change the mineral–melt and/or fluid–melt volatile partition coefficients at the late stages of fractional crystallization.

Effect of pressure and temperature on apatite composition

As apatite–melt halogen–OH exchange coefficients depend on pressure and temperature (Piccoli & Candela, 1994; Riker *et al.*, 2018), mineral compositions may vary, even at a constant melt composition [e.g. equation (2)].

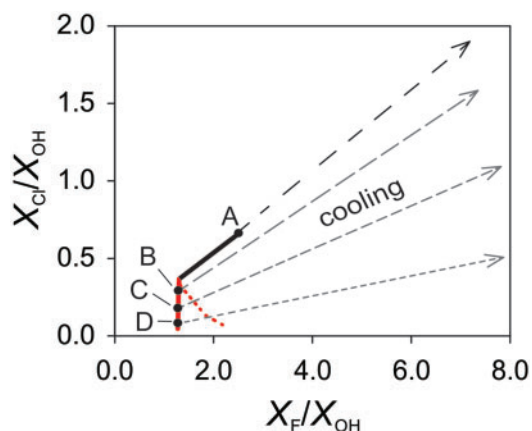


Fig. 10. Effect of re-equilibration on apatite compositions during cooling, shown in binary X_{Cl}/X_{OH} vs X_F/X_{OH} space. The continuous lines represent an arbitrary trend of apatite compositional evolution during volatile-undersaturated (as in Fig. 8b; black line) followed by isobaric H_2O -saturated (as in Fig. 8e; red line) fractional crystallization. The dotted red line illustrates polybaric H_2O -saturated fractional crystallization (as in Fig. 8e). The dashed arrows show modelled trajectories of re-equilibration during cooling from 1000°C to 750°C, starting from different points on the volatile-undersaturated (point A) and isobaric H_2O -saturated (points B–D) trend. In each cooling model, the melt composition is fixed and K_D values are calculated from the P -independent regressions of Riker *et al.* (2018). Cooling of a volatile-undersaturated system, where Cl is retained within the melt (i.e. starting at point A), will cause apatite re-equilibration towards elevated X_{Cl}/X_{OH} and X_F/X_{OH} ratios (black dashed arrow). Extraction of Cl from the melt into the fluid following H_2O -saturation (i.e. starting sequentially from point B to point D) increasingly prevents elevation of X_{Cl}/X_{OH} and drives apatite compositions to high X_F/X_{OH} ratios only (dashed grey lines). Re-equilibration of apatites that grew under volatile-undersaturated conditions to H_2O -saturated conditions could potentially result in intermediate compositions in the space between A–B and B–D.

This is not treated in the fractional crystallization model detailed above but we illustrate the effects of cooling in Fig. 10, using the experimental regression of Riker *et al.* (2018); this is qualitatively consistent with the earlier work of Piccoli & Candela (1994). Cooling drives apatite compositions to higher X_{Cl}/X_{OH} , X_F/X_{OH} and X_F/X_{Cl} ratios, reflecting an increasing preference for the smaller F anion at low temperatures. However, the slope (in binary space) of the cooling trend depends strongly on the Cl concentration of the liquid; at low melt Cl contents, apatite is driven towards high X_F/X_{OH} only (Fig. 10). Pressure has little effect on apatite compositions at constant melt composition (Piccoli & Candela, 1994; Riker *et al.*, 2018), with depressurization primarily allowing a slight increase in the apatite Cl component, which is reflected in a minor decrease in X_F/X_{Cl} and increase in X_{Cl}/X_{OH} ratios.

DISCUSSION

Application of apatite thermodynamic model to Campi Flegrei

The clear differences in model apatite trajectories between H_2O -saturated and volatile-undersaturated

conditions (Fig. 8) suggest that apatite may hold significant clues to understanding the late-stage variations in fluid systematics in magmatic–hydrothermal systems.

Texturally constrained analyses give a temporal dimension to the apatite dataset (Figs 5–7) and analysis of Astroni 1 has shown that the $X_{Halogen}/X_{OH}$ ratios of crystals on the main compositional trend decrease during magmatic evolution (Stock *et al.*, 2016). The same temporal trend is apparent in all eruptions analysed: apatite inclusions trapped in early formed clinopyroxene phenocrysts (*clinopyroxene-in* = 1080°C; Stock *et al.*, 2016) extend to higher $X_{Halogen}/X_{OH}$ ratios than in late-formed biotite phenocrysts (*biotite-in* = 910°C; Stock *et al.*, 2016). Figure 6a–c shows that a good model fit can be achieved with our natural apatite analyses from Campi Flegrei using $K_{Cl-OH}^{Ap/m} = 25$, $K_{F-OH}^{Ap/m} = 75$ and $K_{Cl-F}^{Ap/m} = 0.22$, which are within the range identified experimentally (Riker *et al.*, 2018) and the effects of varying input parameters on the model fit are shown in Figs 8 and 9, and Supplementary Data Figs S3–S6. The model fit (Fig. 6a–c) represents ~70% crystallization at volatile-undersaturated conditions, with constant crystal–melt partition coefficients $\bar{D}_F^{c/m} \approx 0.99$, $\bar{D}_{Cl}^{c/m} \approx 0.8$ and $\bar{D}_{OH}^{c/m} \approx 0.01$ (Fig. 6a–c). These are realistic given the increase in glass halogen concentrations with decreasing MgO and the low modal abundance of apatite and biotite. The low X_{Cl}/X_{OH} values identified in some apatite microphenocrysts can be partially reproduced by subsequent H_2O -saturated crystallization, with $\bar{D}_{Cl}^{f/m} = 20$ and $\bar{D}_F^{f/m} = 0.7$ (Fig. 6a–c), consistent with alkali melt–fluid halogen partitioning experiments under magmatic conditions (Signorelli & Carroll, 2000; Borodulin *et al.*, 2009). However, our simple isobaric, isothermal H_2O -saturated crystallization models cannot reproduce the range of X_F/X_{OH} ratios observed in the natural low X_{Cl}/X_{OH} subsidiary population (Fig. 8d–f). Decompression-induced degassing could account for some of this compositional variability but cooling, after the apatites have re-equilibrated under H_2O -saturated conditions, appears to be the primary mechanism to drive compositions to the very high X_F/X_{OH} ratios observed in some eruptions (e.g. PP; Figs 7 and 10). The second, high X_{Cl}/X_{OH} and X_F/X_{OH} subsidiary population (e.g. Minopoli 1) is consistent with re-equilibration of apatites during cooling of a less degassed melt (Fig. 10).

Pre-eruptive volatile behaviour and the structure of the Campi Flegrei magmatic system

Our models reproduce the main compositional trend in apatite inclusions and microphenocrysts through protracted volatile-undersaturated crystallization (Figs 5–7). This suggests that the main zone of magma storage and crystallization remained volatile-undersaturated until late in magmatic evolution (i.e. after the entrapment of biotite-hosted inclusions; see Stock *et al.*, 2016) prior to past eruptions at Campi Flegrei. Thermodynamic (Rhyolite-MELTS) fractional crystallization models, combined with relevant phonolite

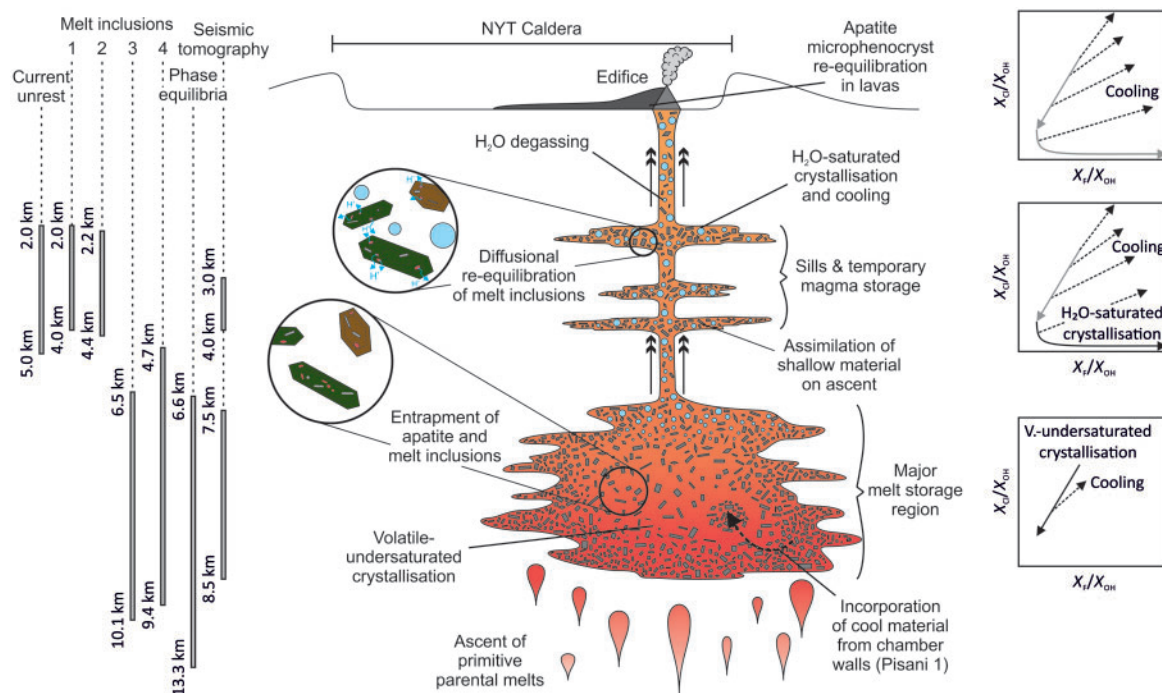


Fig. 11. Schematic diagram summarizing volatile systematics in the Campi Flegrei sub-volcanic plumbing system, based on apatite and glass compositions. The representative graphs (right) illustrate how apatite compositional trends relate to different parts of the magmatic system (black lines show apatite trends that form at a particular depth; grey lines show trends that form at a greater depth but are brought up to shallower levels by ascending magmas). The grey bars (left) display relative estimates of Campi Flegrei magma storage depths, derived from independent constraints: 'current unrest' estimates are from recent ground deformation (Woo & Kilburn, 2010; Amoroso *et al.*, 2014b; D'Auria *et al.*, 2015), fumarolic gas emissions (Carlino *et al.*, 2015) and heat-flow measurements (Di Maio *et al.*, 2015); melt inclusion estimates are for <15 ka eruptions and are from 1—Fourmentraux *et al.* (2012), 2—Vetere *et al.* (2011), 3—Arienzo *et al.* (2016) and 4—Arienzo *et al.* (2010); phase equilibria constraints are from Bohrsen *et al.* (2006), Fowler *et al.* (2007) and Cannatelli (2012); seismic tomography data are from Zollo *et al.* (2008) and De Siena *et al.* (2010). Pressure estimates were converted to depths using a consistent crustal density of 2.3 kg cm^{-3} after Rosi & Sbrana (1987). Not to scale.

solubility data, also show that H_2O would remain undersaturated in Campi Flegrei melts until after *biotite-in* (i.e. $\sim 910^\circ\text{C}$) at pressures $\geq 150 \text{ MPa}$ (Carroll & Blank, 1997; Webster *et al.*, 2014; Stock *et al.*, 2016). Our conclusion that the system remained persistently volatile-undersaturated until a late stage is therefore consistent with independent estimates of Campi Flegrei magma storage conditions, which suggest a high-pressure zone of major melt storage and crystallization (Fig. 11). Seismic tomography shows that the current region of major melt storage beneath Campi Flegrei is $\sim 1 \text{ km}$ thick and at a depth of 7.5 km (Zollo *et al.*, 2008), which would equate to storage pressures of $\sim 170\text{--}190 \text{ MPa}$. This broadly agrees with phase equilibria models, which indicate that mineral and glass compositions produced in past Campi Flegrei eruptions were stable at pressures between 150 and 300 MPa (i.e. $6\text{--}13.3 \text{ km}$; Bohrsen *et al.*, 2006; Fowler *et al.*, 2007; Cannatelli, 2012), and the volatile contents of melt inclusions from <15 ka Campi Flegrei eruptions (Fig. 11), which give saturation pressures up to 229 MPa [$\sim 10 \text{ km}$; Arienzo *et al.*, 2016; using a crustal density of 2.3 g cm^{-3} after Rosi & Sbrana (1987)]. In particular, magma storage depths inferred from melt inclusion volatile contents for the Agnano–Monte Spina (Arienzo *et al.*, 2010) and Nisida

(Arienzo *et al.*, 2016) eruptions overlap at $6.5\text{--}9.4 \text{ km}$, which agrees very well with the current depth of major magma storage ($7.5\text{--}8.5 \text{ km}$; Zollo *et al.*, 2008). This appears to demonstrate that melt storage and crystallization before past eruptions occurred at very similar depths to today.

In addition to the main population of apatite inclusions and microphenocrysts, two subsidiary sets of lower-Cl microphenocrysts are present in some eruptions, as discussed above. Apatites with low $X_{\text{Cl}}/X_{\text{OH}}$ ratios and high $X_{\text{F}}/X_{\text{OH}}$ and $X_{\text{F}}/X_{\text{Cl}}$ ratios (i.e. in Monte Nuovo, Astroni 1, B–FdB, Pisani 1, PP, Minopoli 1; Figs 6 and 7) are consistent with H_2O -saturated fractionation at high $D_{\text{Cl}}^{\text{f/m}}$, where Cl is efficiently extracted from the melt into the fluid phase, but with cooling following extensive fluid exsolution. This requires equilibrating first with low Cl concentrations in the melt owing to degassing, so that any later thermal re-equilibration drives apatites to high $X_{\text{F}}/X_{\text{OH}}$ and $X_{\text{F}}/X_{\text{Cl}}$ only (Fig. 10). The second subsidiary set of apatites, with elevated $X_{\text{Cl}}/X_{\text{OH}}$ and/or $X_{\text{F}}/X_{\text{OH}}$ ratios (i.e. in Astroni 1, B–FdB, PP, Minopoli 1; Figs 6 and 7), are consistent with equilibration during cooling of a melt that is not depleted in Cl (i.e. where Cl has not been extracted into an exsolving fluid; Fig. 10).

These subsidiary compositions represent a small fraction of our dataset, but the analyses are from the cores of microphenocrysts, suggesting that they may have been fully equilibrated under different conditions. In contrast, microphenocrysts that plot on the main trend show no evidence of re-equilibration or overgrowth of new compositions, within the scale of our analyses [Stock *et al.* (2016) checked several grains for compositional zonation within $>16\ \mu\text{m}$ of the rim; although we anticipate that fine-scale zonation might be observable using higher-resolution methods]. The rapid experimental diffusivities of halogens in apatite (Brenan, 1993) suggest that these few anomalous grains must therefore have been spatially separated within the magmatic system. The simplest interpretation of our data is that the low- $X_{\text{Cl}}/X_{\text{OH}}$ apatites represent mushy material left over after incomplete evacuation of magma from separate, shallower storage regions (Fig. 11). Small, melt-rich magma bodies at $\sim 2\text{--}4\text{ km}$ beneath the current Campi Flegrei have been imaged by seismic tomography (De Siena *et al.*, 2010) and inferred from modelling of long-term ground deformation (Amoruso *et al.*, 2014a), fumarolic gas emissions (Carlino *et al.*, 2015) and heat-flow measurements (Di Maio *et al.*, 2015). These shallow magma bodies could derive from emplacement of sills between eruptions; recent seismic crises (1982–1984 and 2011–2013) have been attributed to sill intrusion at 2.75–5 km depth (Fig. 11; Woo & Kilburn, 2010; Amoruso *et al.*, 2014b; D'Auria *et al.*, 2015). Such small, shallow magma bodies would be saturated in volatiles and cooled by interaction with the country rock, allowing microphenocrysts to grow or re-equilibrate. Apatite inclusions, trapped before the magmas were emplaced in the shallow crust, would be 'armoured' by their host phenocrysts, preventing re-equilibration and allowing them to retain their volatile-undersaturated signature. Inclusions that were incompletely enclosed by their host phenocrysts do show evidence of diffusional re-equilibration, manifest as depleted Cl contents relative to fully enclosed inclusions (Stock, 2016). We suggest that magmas ascending from the deep storage region may interact with these shallow melt bodies during eruptions, assimilating some of the residual material and acquiring a mixed cargo of microphenocrysts (Fig. 11). Magmas derived from the deep storage region degassed H_2O during ascent, resulting in low matrix glass H_2O contents (Fig. 4f). Similar F and Cl contents in matrix glasses and melt inclusions (Fig. 4a–d) demonstrate that halogens were not significantly degassed, despite $D_{\text{Cl}}^{f/m} > 1$ (Signorelli & Carroll, 2000). Relatively undepleted matrix glass Cl concentrations are consistent with kinetically induced vapour–melt disequilibrium during rapid ascent (Webster *et al.*, 1993; Barclay *et al.*, 1996; Shea *et al.*, 2014).

The apatite microphenocrysts from Pisani 1 that branch away from the main population at moderate $X_{\text{Cl}}/X_{\text{OH}}$ are consistent with cooling (Fig. 10), but before any H_2O -saturated crystallization has taken place. We

suggest that these crystals formed in the main magma storage region at depth, possibly in cooler regions of the reservoir (e.g. close to the walls) and were incorporated before eruption (Fig. 11).

The majority of apatite inclusions and microphenocrysts from B–FdB are compositionally distinct, with significantly lower Cl contents than other explosive eruptions (Figs 5 and 7a–c). This could be explained if part of the B–FdB magma crystallized from a melt with a different initial volatile content (i.e. lower Cl, higher H_2O ; Fig. 9a and b). The B–FdB eruption occurred at the start of Epoch 2 after a long hiatus in activity (Smith *et al.*, 2011), and may have assimilated some of the country rock surrounding its magma reservoir during this time. Large volumes of residue from the Campanian Ignimbrite magma chamber underlie the Campi Flegrei caldera (D'Antonio, 2011) and represent a potential assimilate. Melt inclusions from the Campanian Ignimbrite extend to high H_2O contents and Campanian Ignimbrite glasses are consistently Cl-deficient compared with eruptions in the past 15 kyr (see Fig. 4a and b; Signorelli *et al.*, 1999; Marianelli *et al.*, 2006). Furthermore, B–FdB glasses are depleted in Sr and Ba and enriched in Zr relative to other $<15\text{ ka}$ eruptions (Smith *et al.*, 2011), again suggesting possible contamination from older ($>15\text{ ka}$) Campi Flegrei eruptions, including the Campanian Ignimbrite (Tomlinson *et al.*, 2012).

Apatite microphenocrysts from Accademia and SMdG lava samples are distinct from those in explosive deposits. They do not show the same compositional trend of F–OH exchange with an approximately constant Cl, but rather define a trend with an increasing F component at the expense of Cl, curving first towards the F–Cl binary and then towards the F apex (Fig. 6g–i). This is analogous to the modelled trend of apatite compositional evolution during cooling. However, in binary space, apatite microphenocrysts from lava deposits are scattered with no discernible trend. We interpret this as variable extents of diffusive re-equilibration in the lavas (Fig. 10). Although microphenocrysts plot on the same cooling trend, they have different starting points and have variably rehomogenized. Such extensive re-equilibration of microphenocryst compositions is unique to lava samples and we interpret that it occurred during slow cooling of the host magma at or near the surface (Fig. 11).

Apatite inclusions in clinopyroxene and biotite record volatile-undersaturated crystallization (see above) and we would therefore expect the H_2O contents of melt inclusions in the same phenocryst phases to correlate negatively with MgO, as H_2O behaves incompatibly during magmatic evolution. However, there is no correlation between clinopyroxene-hosted melt inclusion H_2O and MgO concentrations in any of the analysed eruptions, and most melt inclusions measured in this study contain $\sim 2.0\text{--}3.8\text{ wt \% H}_2\text{O}$ (Fig. 4e). This may indicate that melt inclusion H_2O contents have been reset after entrapment, reflecting the final (H_2O -saturated)

equilibration pressure at shallow crustal levels. Rapid H^+ diffusion through common phenocrysts causes re-equilibration of melt inclusion H_2O concentrations on short timescales (potentially hours to weeks under magmatic conditions) in response to any change in external conditions (e.g. Woods *et al.*, 2000; Ingrin & Blanchard, 2006; Reubi *et al.*, 2013). In contrast, re-equilibration of apatite inclusions would be inhibited by the need for coupled halogen diffusion to retain stoichiometry (Bucholz *et al.*, 2013). Occasional volatile-rich melt inclusions in <15 ka Campi Flegrei deposits attest to evolved melts at depth (i.e. ≥ 5 wt % H_2O in Fig. 4e).

Campi Flegrei melt inclusions consistently have very low CO_2 contents (e.g. Marianelli *et al.*, 2006; Arienzo *et al.*, 2010; Stock *et al.*, 2016), so we used a polynomial regression through published 850–950°C, CO_2 -free phonolite and trachyte solubility data (Carroll & Blank, 1997; Di Matteo *et al.*, 2004; Larsen & Gardner, 2004; Schmidt & Behrens, 2008; Webster *et al.*, 2014) to estimate a saturation pressure of ~24–76 MPa for the degassed melt inclusions (2.0–3.8 wt % H_2O). This is equivalent to storage depths of ~1.1–3.4 km, which coincide with the depth of small, melt-rich magma bodies imaged beneath the current Campi Flegrei caldera (~2–4 km; De Siena *et al.*, 2010). We infer that ascending magmas interacted with these shallow melt bodies during eruption, stalling or slowing such that melt inclusions from the deep reservoir re-equilibrated (Fig. 11), and incorporating phenocrysts with degassed melt inclusions (along with apatite microphenocrysts), which were stored in this shallow crystal residue.

Inter-eruption variability in pre-eruptive magma volatile contents

Our data generally show the same qualitative trends in apatite inclusion and microphenocryst compositions in explosive eruptions, regardless of the erupted volume, melt composition or epoch of activity. The majority of apatite inclusions and microphenocrysts plot on a trend that is consistent with volatile-undersaturated fractionation. However, in different eruptions, this main apatite trend is offset depending on the epoch of activity, suggesting a temporal variation in melt volatile composition. This is particularly evident in SIMS data, which are more precise than the EPMA data. For example, apatite inclusions from Astroni 1 (Epoch 3) and the historical Monte Nuovo eruptions are typically F-rich and OH-depleted with higher $X_{Halogen}/X_{OH}$ ratios than those in Epoch 1 (Minopoli 1, PP, Pisani 1; Fig. 5). The same is true for microphenocrysts, except that microphenocrysts from Monte Nuovo cover the entire compositional range measured in other eruptions (Figs 6 and 7). Epoch 2 (B–FdB) crystals have similar X_C/X_{OH} ratios to those from Epoch 1 but cannot be compared directly given their distinct compositional trajectory (Fig. 7b and c).

Melt inclusion halogen contents are typically lower in Epoch 1 than in later explosive eruptions (Fig. 4a and

c), consistent with the more primitive Epoch 1 major element glass compositions (Figs 2 and 3). As $\bar{D}_F^{c/m} > \bar{D}_{Cl}^{c/m} > \bar{D}_{H_2O}^{c/m}$ during apatite crystallization (see Supplementary Data), we would anticipate melt H_2O contents to be proportionally lower for Epoch 1 magmas. Consequently, we would expect apatites forming from the more primitive Epoch 1 magmas to have higher $X_{Halogen}/X_{OH}$ than those forming from Epoch 3 magmas, the opposite to what is observed (Fig. 5). This disparity can be explained by a systematic difference in the melt volatile composition at the point of initial apatite crystallization (i.e. *apatite-in*; C_1^0), changing apatite compositions without significantly affecting mineral phase stabilities or the trajectory of apatite compositional evolution. Specifically, the change to higher $X_{Halogen}/X_{OH}$ in Astroni 1 (Epoch 3) and Monte Nuovo suggests a decrease in melt H_2O concentrations at *apatite-in* ($C_{H_2O}^0$) relative to Epoch 1 (Fig. 9a and b). At Campi Flegrei, Rhyolite-MELTS models demonstrate that $C_{H_2O}^0$ depends on the H_2O content of the melt at the liquidus, and does not change significantly as a result of variations in pressure or oxygen fugacity (Stock *et al.*, 2016). Variability in Campi Flegrei apatite compositions from different epochs is therefore likely to reflect temporal variations in the H_2O concentration of parental melts feeding the system; Epoch 1 parental melts have higher apparent H_2O contents than more recent eruptions. This agrees with isotopic evidence, which suggests that Epochs 1 and 2 were fed by the ‘Minopoli 2’ and ‘NYT’ end-members (i.e. a high slab-derived fluid and/or low subducted sediment mantle wedge input) primitive melts, whereas Epoch 3 and Monte Nuovo melts include the ‘Astroni 6 end-member’ component (i.e. a reduced slab-derived fluid and/or low subducted sediment mantle wedge input; D’Antonio *et al.*, 2007; Di Renzo *et al.*, 2011).

CONCLUSIONS

Apatite analysis represents a robust approach for assessing magmatic volatile behaviour that has many major advantages over established techniques (e.g. melt inclusion analysis). Apatite microphenocrysts remain in equilibrium with their host melts on geologically short timescales but are unable to re-equilibrate on very short timescales during magma ascent. In contrast, apatite inclusions are isolated from the magma on entrapment and preserve a record of conditions earlier in crystallization. In explosive Campi Flegrei eruptions, apatite inclusions record persistent volatile-undersaturated conditions until late in the crystallization history of the evolving magma, interpreted to occur in a deep magma reservoir at ~7.5–8.5 km, which corresponds with the current depth of major magma storage at Campi Flegrei. In addition to this main volatile-undersaturated trend, apatite microphenocrysts also display subsidiary trends, related to cooling and H_2O -saturated crystallization. The compositional diversity of

apatite microphenocrysts is consistent with a mixed crystal cargo, attained as melts ascending from depth interact with crystal residue in discrete shallow-crustal magma bodies. Clinopyroxene-hosted melt inclusion H₂O contents from Campi Flegrei commonly record saturation pressures equating to 1–3 km depth, owing to incorporation of phenocrysts that have been stored in the shallow crust and/or stalling of ascending magmas as they interact with shallow crustal magma bodies. This corresponds with small melt zones imaged seismically beneath the current Campi Flegrei caldera and the depth of sill emplacement during recent seismic crises. In lava deposits, apatite microphenocrysts diffusively re-equilibrate during cooling at the surface. A systematic offset in volatile-undersaturated apatite compositions between eruptions suggests that the H₂O content of parental melts feeding the system was higher in Epoch 1 than in more recent times (i.e. Epoch 3 and Monte Nuovo). Although we have focused on Campi Flegrei, our approach of comparing thermodynamic models of apatite compositional evolution with empirical analyses can be applied widely to determine the temporal evolution of pre-eruptive volatile behaviour in other volcanic systems, providing new perspectives on sub-volcanic processes.

ACKNOWLEDGEMENTS

We thank Richard Hinton, Norman Charnley and Stuart Kearns for analytical assistance and advice, Roel van Elsas for support in mineral separation, and Dan Harlov for generously providing synthetic apatite standard materials. Jason Coumans wrote a MATLAB version of the thermodynamic model, which helped in defining the different crystallization scenarios. The paper was greatly improved by thorough, constructive reviews from Massimo D'Antonio, Richard Hervig and an anonymous reviewer, and we are grateful to Georg Zellmer for editorial handling. We thank Jenni Barclay and Lars Hansen for their comments on an early version of this paper, and Jim Webster, Jenny Riker and Jon Wade for their valuable feedback and discussion.

FUNDING

M.J.S. was supported by a NERC studentship (NE/K500811/01) and a Junior Research Fellowship from Christ's College, Cambridge. M.C.S.H. was supported by a Royal Society University Research Fellowship. M.C.S.H., V.C.S. and R.A.B. acknowledge funding from a NERC grant (NE/K003852/1). SIMS analysis was funded by a NERC Edinburgh Ion Microprobe Facility grant (IMF519/0514).

SUPPLEMENTARY DATA

Supplementary data for this paper are available at *Journal of Petrology* online.

REFERENCES

- Amoruso, A., Crescentini, L. & Sabetta, I. (2014a). Paired deformation sources of the Campi Flegrei caldera (Italy) required by recent (1980–2010) deformation history. *Journal of Geophysical Research: Solid Earth* **119**, 858–879.
- Amoruso, A., Crescentini, L., Sabetta, I., De Martino, P., Obrizzo, F. & Tammaro, U. (2014b). Clues to the cause of the 2011–2013 Campi Flegrei caldera unrest, Italy, from continuous GPS data. *Geophysical Research Letters* **41**, 3081–3088.
- Annen, C., Blundy, J. D. & Sparks, R. S. J. (2006). The genesis of intermediate and silicic magmas in deep crustal hot zones. *Journal of Petrology* **47**, 505–539.
- Arienzo, I., Moretti, R., Civetta, L., Orsi, G. & Papale, P. (2010). The feeding system of Agnano–Monte Spina eruption (Campi Flegrei, Italy): dragging the past into present activity and future scenarios. *Chemical Geology* **270**, 135–147.
- Arienzo, I., Mazzeo, F. C., Moretti, R., Cavallo, A. & D'Antonio, M. (2016). Open-system magma evolution and fluid transfer at Campi Flegrei caldera (Southern Italy) during the past 5 ka as revealed by geochemical and isotopic data: The example of the Nisida eruption. *Chemical Geology* **427**, 109–124.
- Arzilli, F., Piochi, M., Mormone, A., Agostini, C. & Carroll, M. R. (2016). Constraining pre-eruptive magma conditions and unrest timescales during the Monte Nuovo eruption (1538 AD; Campi Flegrei, Southern Italy): integrating textural and CSD results from experimental and natural trachy-phonolites. *Bulletin of Volcanology* **78**, 72.
- Barclay, J., Carroll, M. R., Houghton, B. F. & Wilson, C. J. N. (1996). Pre-eruptive volatile content and degassing history of an evolving peralkaline volcano. *Journal of Volcanology and Geothermal Research* **74**, 75–87.
- Bevilacqua, A., Flandoli, F., Neri, A., Isaia, R. & Vitale, S. (2016). Temporal models for the episodic volcanism of Campi Flegrei caldera (Italy) with uncertainty quantification. *Journal of Geophysical Research: Solid Earth* **121**, 7821–7845.
- Bohrson, W. A., Spera, F. J., Fowler, S. J., Belkin, H. E., De Vivo, B. & Rolandi, G. (2006). Petrogenesis of the Campanian ignimbrite: implications for crystal–melt separation and open-system processes from major and trace elements and Th isotopic data. *Developments in Volcanology* **9**, 249–288.
- Borodulin, G. P., Chevychelov, V. Y. & Zaraysky, G. P. (2009). Experimental study of partitioning of tantalum, niobium, manganese, and fluorine between aqueous fluoride fluid and granitic and alkaline melts. *Doklady Earth Sciences* **427**, 868–873.
- Boyce, J. W. & Hervig, R. L. (2009). Apatite as a monitor of late-stage magmatic processes at Volcán Irazú, Costa Rica. *Contributions to Mineralogy and Petrology* **157**, 135–145.
- Boyce, J. W., Tomlinson, S. M., McCubbin, F. M., Greenwood, J. P. & Treiman, A. H. (2014). The lunar apatite paradox. *Science* **344**, 400–402.
- Brenan, J. (1993). Kinetics of fluorine, chlorine and hydroxyl exchange in fluorapatite. *Chemical Geology* **110**, 195–210.
- Bucholz, C. E., Gaetani, G. A., Behn, M. D. & Shimizu, N. (2013). Post-entrapment modification of volatiles and oxygen fugacity in olivine-hosted melt inclusions. *Earth and Planetary Science Letters* **374**, 145–155.
- Candela, P. A. (1986). Toward a thermodynamic model for the halogens in magmatic systems: an application to melt–vapour–apatite equilibria. *Chemical Geology* **57**, 289–301.
- Candela, P. A. & Holland, H. D. (1986). A mass transfer model for copper and molybdenum in magmatic hydrothermal systems: the origin of porphyry-type ore deposits. *Economic Geology* **81**, 1–19.
- Cannatelli, C. (2012). Understanding magma evolution at Campi Flegrei (Campania, Italy) volcanic complex using

- melt inclusions and phase equilibria. *Mineralogy and Petrology* **104**, 29–42.
- Cannatelli, C., Lima, A., Bodnar, R. J., De Vivo, B., Webster, J. D. & Fedele, L. (2007). Geochemistry of melt inclusions from the Fondo Riccio and Minopoli 1 eruptions at Campi Flegrei (Italy). *Chemical Geology* **237**, 418–432.
- Carlino, S., Kilburn, C. R. J., Tramelli, A., Troise, C., Somma, R. & De Natale, G. (2015). Tectonic stress and renewed uplift at Campi Flegrei caldera, southern Italy: new insights from caldera drilling. *Earth and Planetary Science Letters* **420**, 23–29.
- Carroll, M. R. & Blank, J. G. (1997). The solubility of H₂O in phonolitic melts. *American Mineralogist* **82**, 549–556.
- Cashman, K. V. (2004). Volatile controls on magma ascent and eruption. In: Sparks, R. S. J. & Hawkesworth, C. J. (eds) *The State of the Planet: Frontiers and Challenges in Geophysics. American Geophysical Union, Geophysical Monograph* **150**, 109–124.
- Chiodini, G., Caliro, S., De Martino, P., Avino, R. & Gherardi, F. (2012). Early signals of new volcanic unrest at Campi Flegrei caldera? Insights from geochemical data and physical simulations. *Geology* **40**, 943–946.
- Cioni, R., Marianelli, P. & Santacroce, R. (1998). Thermal and compositional evolution of the shallow magma chambers of Vesuvius: evidence from pyroxene phenocrysts and melt inclusions. *Journal of Geophysical Research: Solid Earth* **103**, 18277–18294.
- Civetta, L., Carluccio, E., Innocenti, F., Sbrana, A. & Taddeucci, G. (1991). Magma chamber evolution under the Phlegraean Fields during the last 10 ka: trace element and isotope data. *European Journal of Mineralogy* **3**, 415–428.
- D'Antonio, M. (2011). Lithology of the basement underlying the Campi Flegrei caldera: volcanological and petrological constraints. *Journal of Volcanology and Geothermal Research* **200**, 91–98.
- D'Antonio, M., Civetta, L., Orsi, G., Pappalardo, L., Piochi, M., Carandente, A., De Vita, S., Di Vito, M. & Isaia, R. (1999). The present state of the magmatic system of the Campi Flegrei caldera based on a reconstruction of its behavior in the past 12 ka. *Journal of Volcanology and Geothermal Research* **91**, 247–268.
- D'Antonio, M., Tonarini, S., Arienzo, I., Civetta, L. & Di Renzo, V. (2007). Components and processes in the magma genesis of the Phlegraean Volcanic District, southern Italy. In: Beccaluva, L., Bianchini, G. & Wilson, M. (eds) *Cenozoic Volcanism in the Mediterranean Area. Geological Society of America, Special Papers* **418**, 203–220.
- D'Auria, L., Pepe, S., Castaldo, R., Giudicepietro, F., Macedonio, G., Ricciolino, P., Tizzani, P., Casu, F., Lanari, R. & Manzo, M. (2015). Magma injection beneath the urban area of Naples: a new mechanism for the 2012–2013 volcanic unrest at Campi Flegrei caldera. *Scientific Reports* **5**, article number 13100.
- Danyushevsky, L. V., McNeill, A. W. & Sobolev, A. V. (2002). Experimental and petrological studies of melt inclusions in phenocrysts from mantle-derived magmas: an overview of techniques, advantages and complications. *Chemical Geology* **183**, 5–24.
- Deino, A. L., Orsi, G., de Vita, S. & Piochi, M. (2004). The age of the Neapolitan Yellow Tuff caldera-forming eruption (Campi Flegrei caldera—Italy) assessed by ⁴⁰Ar/³⁹Ar dating method. *Journal of Volcanology and Geothermal Research* **133**, 157–170.
- De Siena, L., Del Pezzo, E. & Bianco, F. (2010). Seismic attenuation imaging of Campi Flegrei: evidence of gas reservoirs, hydrothermal basins, and feeding systems. *Journal of Geophysical Research* **115**, B09312.
- Dietterich, H. & de Silva, S. (2010). Sulfur yield of the 1600 eruption of Huaynaputina, Peru: Contributions from magmatic, fluid-phase, and hydrothermal sulfur. *Journal of Volcanology and Geothermal Research* **197**, 303–312.
- Di Maio, R., Piegari, E., Mancini, C. & Scandone, R. (2015). Numerical study of conductive heat losses from a magmatic source at Phlegraean Fields. *Journal of Volcanology and Geothermal Research* **290**, 75–81.
- Di Matteo, V., Carroll, M. R., Behrens, H., Vetere, F. & Brooker, R. A. (2004). Water solubility in trachytic melts. *Chemical Geology* **213**, 187–196.
- Di Renzo, V., Arienzo, I., Civetta, L., D'Antonio, M., Tonarini, S., Di Vito, M. A. & Orsi, G. (2011). The magmatic feeding system of the Campi Flegrei caldera: architecture and temporal evolution. *Chemical Geology* **281**, 227–241.
- Di Vito, M. A., Isaia, R., Orsi, G., Southon, J., de Vita, S., D'Antonio, M., Pappalardo, L. & Piochi, M. (1999). Volcanism and deformation since 12,000 years at the Campi Flegrei caldera (Italy). *Journal of Volcanology and Geothermal Research* **91**, 221–246.
- Di Vito, M. A., Arienzo, I., Braia, G., Civetta, L., D'Antonio, M., Di Renzo, V. & Orsi, G. (2011). The Averno 2 fissure eruption: a recent small-size explosive event at the Campi Flegrei Caldera (Italy). *Bulletin of Volcanology* **73**, 295–320.
- Dunbar, N. W., Hervig, R. L. & Kyle, P. R. (1989). Determination of pre-eruptive H₂O, F and Cl contents of silicic magmas using melt inclusions: examples from Taupo volcanic center, New Zealand. *Bulletin of Volcanology* **51**, 177–184.
- Edmonds, M. (2008). New geochemical insights into volcanic degassing. *Philosophical Transactions of the Royal Society of London, Series A* **366**, 4559–4579.
- Fourmentaux, C., Métrich, N., Bertagnini, A. & Rosi, M. (2012). Crystal fractionation, magma step ascent, and syn-eruptive mingling: the Averno 2 eruption (Phlegraean Fields, Italy). *Contributions to Mineralogy and Petrology* **163**, 1121–1137.
- Fowler, S. J., Spera, F. J., Bohrsen, W. A., Belkin, H. E. & De Vivo, B. (2007). Phase equilibria constraints on the chemical and physical evolution of the Campanian Ignimbrite. *Journal of Petrology* **48**, 459–493.
- Gaetani, G. A., O'Leary, J. A., Shimizu, N., Bucholz, C. E. & Newville, M. (2012). Rapid reequilibration of H₂O and oxygen fugacity in olivine-hosted melt inclusions. *Geology* **40**, 915–918.
- Giaccio, B., Hajdas, I., Isaia, R., Deino, A. & Nomade, S. (2017). High-precision ¹⁴C and ⁴⁰Ar/³⁹Ar dating of the Campanian Ignimbrite (Y-5) reconciles the time-scales of climatic-cultural processes at 40 ka. *Scientific Reports* **7**, article number 45940.
- Giordano, D., Russell, J. K. & Dingwell, D. B. (2008). Viscosity of magmatic liquids: a model. *Earth and Planetary Science Letters* **271**, 123–134.
- Goldoff, B., Webster, J. D. & Harlov, D. E. (2012). Characterization of fluor-chlorapatites by electron probe microanalysis with a focus on time-dependent intensity variation of halogens. *American Mineralogist* **97**, 1103–1115.
- Grove, T. L., Elkins-Tanton, L. T., Parman, S. W., Chatterjee, N., Müntener, O. & Gaetani, G. A. (2003). Fractional crystallization and mantle-melting controls on calc-alkaline differentiation trends. *Contributions to Mineralogy and Petrology* **145**, 515–533.
- Humphreys, M. C. S., Kearns, S. L. & Blundy, J. D. (2006). SIMS investigation of electron-beam damage to hydrous, rhyolitic glasses: Implications for melt inclusion analysis. *American Mineralogist* **91**, 667–679.
- Huppert, H. E. & Woods, A. W. (2002). The role of volatiles in magma chamber dynamics. *Nature* **420**, 493–495.
- Ingrin, J. & Blanchard, M. (2006). Diffusion of hydrogen in minerals. In: Keppler, H. & Smyth, J. R. (eds) *Water in Nominally Anhydrous Minerals. Mineralogical Society of America and Geochemical Society, Reviews in Mineralogy and Geochemistry* **62**, 291–320.

- Isaia, R., D'Antonio, M., Dell'Erba, F., Di Vito, M. & Orsi, G. (2004). The Astroni volcano: the only example of closely spaced eruptions in the same vent area during the recent history of the Campi Flegrei caldera (Italy). *Journal of Volcanology and Geothermal Research* **133**, 171–192.
- Isaia, R., Marianelli, P. & Sbrana, A. (2009). Caldera unrest prior to intense volcanism in Campi Flegrei (Italy) at 4.0 ka BP: Implications for caldera dynamics and future eruptive scenarios. *Geophysical Research Letters* **36**, L21303.
- Lange, R. L. & Carmichael, I. S. E. (1990). Thermodynamic properties of silicate liquids with emphasis on density, thermal expansion and compressibility. In: Nicholls, J. & Russell, J. K. (eds) *Modern Methods of Igneous Petrology: Understanding Magmatic Processes*. Mineralogical Society of America, *Reviews in Mineralogy* **24**, 25–64.
- Larsen, J. F. & Gardner, J. E. (2004). Experimental study of water degassing from phonolite melts: implications for volatile oversaturation during magmatic ascent. *Journal of Volcanology and Geothermal Research* **134**, 109–124.
- Li, H. & Hermann, J. (2017). Chlorine and fluorine partitioning between apatite and sediment melt at 2.5 GPa, 800°C: A new experimentally derived thermodynamic model. *American Mineralogist* **102**, 580–594.
- Lloyd, A. S., Plank, T., Ruprecht, P., Hauri, E. H. & Rose, W. (2013). Volatile loss from melt inclusions in pyroclasts of differing sizes. *Contributions to Mineralogy and Petrology* **165**, 129–153.
- Mangiaccapra, A., Moretti, R., Rutherford, M., Civetta, L., Orsi, G. & Papale, P. (2008). The deep magmatic system of the Campi Flegrei caldera (Italy). *Geophysical Research Letters* **35**, L21304.
- Marianelli, P., Sbrana, A. & Proto, M. (2006). Magma chamber of the Campi Flegrei supervolcano at the time of eruption of the Campanian Ignimbrite. *Geology* **34**, 937–940.
- Mastrolorenzo, G. & Pappalardo, L. (2006). Magma degassing and crystallization processes during eruptions of high-risk Neapolitan-volcanoes: evidence of common equilibrium rising processes in alkaline magmas. *Earth and Planetary Science Letters* **250**, 164–181.
- McCubbin, F. M., Jolliff, B. L., Nekvasil, H., Carpenter, P. K., Zeigler, R. A., Steele, A., Elardo, S. M. & Lindsley, D. H. (2011). Fluorine and chlorine abundances in lunar apatite: implications for heterogeneous distributions of magmatic volatiles in the lunar interior. *Geochimica et Cosmochimica Acta* **75**, 5073–5093.
- McCubbin, F. M., Kaden, K. E. V., Tartèse, R., Boyce, J. W., Mikhail, S., Whitson, E. S., Bell, A. S., Anand, M., Franchi, I. A., Wang, J. & Hauri, E. H. (2015). Experimental investigation of F, Cl, and OH partitioning between apatite and Fe-rich basaltic melt at 1.0–1.2 GPa and 950–1000°C. *American Mineralogist* **100**, 1790–1802.
- Melluso, L., Morra, V., Perrotta, A., Scarpati, C. & Adabbo, M. (1995). The eruption of the Breccia Museo (Campi Flegrei, Italy): Fractional crystallization processes in a shallow, zoned magma chamber and implications for the eruptive dynamics. *Journal of Volcanology and Geothermal Research* **68**, 325–339.
- Melluso, L., De'Gennaro, R., Fedele, L., Franciosi, L. & Morra, V. (2012). Evidence of crystallization in residual, Cl-F-rich, agpaitic, trachyphonolitic magmas and primitive Mg-rich basalt-trachyphonolite interaction in the lava domes of the Phlegrean Fields (Italy). *Geological Magazine* **149**, 532–550.
- Moore, L., Gazel, E., Tuohy, R., Lloyd, A., Esposito, R., Steele-MacInnis, M., Hauri, E. H., Wallace, P. J., Plank, T. & Bodnar, R. J. (2015). Bubbles matter: an assessment of the contribution of vapour bubbles to melt inclusion volatile budgets. *American Mineralogist* **100**, 806–823.
- Moretti, R., De Natale, G. & Troise, C. (2017). A geochemical and geophysical reappraisal to the significance of the recent unrest at Campi Flegrei caldera (Southern Italy). *Geochemistry, Geophysics, Geosystems* **18**, 1244–1269.
- Pan, Y. & Fleet, M. E. (2002). Compositions of the apatite-group minerals: substitution mechanisms and controlling factors. In: Kohn, M. L., Rakovan, J. & Hughes, J. M. (eds) *Phosphates—Geochemical, Geobiological, and Materials Importance*. Mineralogical Society of America and Geochemical Society, *Reviews in Mineralogy and Geochemistry* **48**, 13–49.
- Pappalardo, L., Civetta, L., d'Antonio, M., Deino, A., Di Vito, M., Orsi, G., Carandente, A., De Vita, S., Isaia, R. & Piochi, M. (1999). Chemical and Sr-isotopic evolution of the Phlegraean magmatic system before the Campanian Ignimbrite and the Neapolitan Yellow Tuff eruptions. *Journal of Volcanology and Geothermal Research* **91**, 141–166.
- Pappalardo, L., Piochi, M., D'Antonio, M., Civetta, L. & Petrini, R. (2002). Evidence for multi-stage magmatic evolution during the past 60 kyr at Campi Flegrei (Italy) deduced from Sr, Nd and Pb isotope data. *Journal of Petrology* **43**, 1415–1434.
- Patiño Douce, A. E. & Roden, M. (2006). Apatite as a probe of halogen and water fugacities in the terrestrial planets. *Geochimica et Cosmochimica Acta* **70**, 3173–3196.
- Piccoli, P. & Candela, P. (1994). Apatite in felsic rocks: a model for the estimation of initial halogen concentrations in the Bishop Tuff (Long Valley) and Tuolumne Intrusive Suite (Sierra Nevada Batholith) magmas. *American Journal of Science* **294**, 92–135.
- Piccoli, P. M. & Candela, P. A. (2002). Apatite in igneous systems. In: Kohn, M. L., Rakovan, J. & Hughes, J. M. (eds) *Phosphates—Geochemical, Geobiological, and Materials Importance*. Mineralogical Society of America and Geochemical Society, *Reviews in Mineralogy and Geochemistry* **48**, 255–292.
- Piochi, M., Mastrolorenzo, G. & Pappalardo, L. (2005). Magma ascent and eruptive processes from textural and compositional features of Monte Nuovo pyroclastic products, Campi Flegrei, Italy. *Bulletin of Volcanology* **67**, 663–678.
- Pistolesi, M., Bertagnini, A., Di Roberto, A., Isaia, R., Vona, A., Cioni, R. & Giordano, G. (2017). The Baia-Fondi di Baia eruption at Campi Flegrei: stratigraphy and dynamics of a multi-stage caldera reactivation event. *Bulletin of Volcanology* **79**, 67.
- Portnyagin, M., Almeev, R., Matveev, S. & Holtz, F. (2008). Experimental evidence for rapid water exchange between melt inclusions in olivine and host magma. *Earth and Planetary Science Letters* **272**, 541–552.
- Preece, K., Gertisser, R., Barclay, J., Berlo, K., Herd, R. A. & EIMF (2014). Pre- and syn-eruptive degassing and crystallisation processes of the 2010 and 2006 eruptions of Merapi volcano, Indonesia. *Contributions to Mineralogy and Petrology* **168**, 1061.
- Pyle, J. M., Spear, F. S. & Wark, D. A. (2002). Electron microprobe analysis of REE in apatite, monazite and xenotime: protocols and pitfalls. In: Kohn, M. L., Rakovan, J. & Hughes, J. M. (eds) *Phosphates—Geochemical, Geobiological, and Materials Importance*. Mineralogical Society of America and Geochemical Society, *Reviews in Mineralogy and Geochemistry* **48**, 337–362.
- Reimer, P. J., Bard, E., Bayliss, A., Beck, J. W., Blackwell, P. G., Bronk Ramsey, C., Buck, C. E., Cheng, H., Edwards, R. L., Friedrich, M., Grootes, P. M., Guilderson, T. P., Hafflidason, H., Hajdas, I., Hatté, C., Heaton, T., Hoffmann, D. L., Hogg, A. G., Hughen, K. A., Kaiser, K. F., Kromer, B., Manning, S. W., Niu, M., Reimer, R. W., Richards, D. A., Scott, E. M.,

- Southon, J. R., Staff, R. A., Turney, C. S. M. & van der Plicht, J. (2013). IntCal13 and Marine13 radiocarbon age calibration curves 0–50,000 years cal BP. *Radiocarbon* **55**, 1869–1887.
- Reubi, O., Blundy, J. & Varley, N. R. (2013). Volatiles contents, degassing and crystallisation of intermediate magmas at Volcan de Colima, Mexico, inferred from melt inclusions. *Contributions to Mineralogy and Petrology* **165**, 1087–1106.
- Riker, J., Humphreys, M. C., Brooker, R. A., De Hoog, J. C. & EIMF (2018). First measurements of OH-C exchange and temperature-dependent partitioning of OH and halogens in the system apatite–silicate melt. *American Mineralogist* **103**, 260–270.
- Roggensack, K., Hervig, R. L., McKnight, S. B. & Williams, S. N. (1997). Explosive basaltic volcanism from Cerro Negro volcano: influence of volatiles on eruptive style. *Science* **277**, 1639–1642.
- Rosi, M. & Sbrana, A. (1987). *The Phlegrean Fields*. CNR, Quaderni di la Ricerca Scientifica **114**, 175 pp.
- Saal, A. E., Hauri, E. H., Langmuir, C. H. & Perfit, M. R. (2002). Vapour undersaturation in primitive mid-ocean-ridge basalt and the volatile content of Earth's upper mantle. *Nature* **419**, 451–455.
- Schmidt, B. C. & Behrens, H. (2008). Water solubility in phonolite melts: Influence of melt composition and temperature. *Chemical Geology* **256**, 259–268.
- Shea, T., Hellebrand, E., Gurioli, L. & Tuffen, H. (2014). Conduit to localized-scale degassing during Plinian eruptions: insights from major element and volatile (Cl and H₂O) analyses within Vesuvius AD 79 pumice. *Journal of Petrology* **55**, 315–344.
- Signorelli, S. & Carroll, M. R. (2000). Solubility and fluid–melt partitioning of Cl in hydrous phonolitic melts. *Geochimica et Cosmochimica Acta* **64**, 2851–2862.
- Signorelli, S., Vaggelli, G., Francalanci, L. & Rosi, M. (1999). Origin of magmas feeding the Plinian phase of the Campanian Ignimbrite eruption, Phlegrean Fields (Italy): constraints based on matrix-glass and glass-inclusion compositions. *Journal of Volcanology and Geothermal Research* **91**, 199–220.
- Smith, V. C., Isaia, R. & Pearce, N. J. G. (2011). Tephrostratigraphy and glass compositions of post-15 kyr Campi Flegrei eruptions: implications for eruption history and chronostratigraphic markers. *Quaternary Science Reviews* **30**, 3638–3660.
- Stefano, C. J., Mukasa, S. B., Andronikov, A. & Leeman, W. P. (2011). Water and other volatile systematics of olivine-hosted melt inclusions from the Yellowstone hotspot track. *Contributions to Mineralogy and Petrology* **161**, 615–633.
- Stock, M. J. (2016). The volatile history of past volcanic eruptions. PhD thesis, University of Oxford.
- Stock, M. J., Humphreys, M. C. S., Smith, V. C., Johnson, R. D., Pyle, D. M. & EIMF (2015). New constraints on electron-beam induced halogen migration in apatite. *American Mineralogist* **100**, 281–293.
- Stock, M. J., Humphreys, M. C. S., Smith, V. C., Isaia, R. & Pyle, D. M. (2016). Late-stage volatile saturation as a potential trigger for explosive volcanic eruptions. *Nature Geoscience* **9**, 249–254.
- Stormer, J. C., Pierson, M. L. & Tacker, R. C. (1993). Variation of F and Cl X-ray intensity due to anisotropic diffusion in apatite. *American Mineralogist* **78**, 641–648.
- Tomlinson, E. L., Arienzo, I., Civetta, L., Wulf, S., Smith, V. C., Hardiman, M., Lane, C. S., Carandente, A., Orsi, G., Rosi, M., Müller, W. & Menzies, M. A. (2012). Geochemistry of the Phlegrean Fields (Italy) proximal sources for major Mediterranean tephra: Implications for the dispersal of Plinian and co-ignimbritic components of explosive eruptions. *Geochimica et Cosmochimica Acta* **93**, 102–128.
- Tonarini, S., Leeman, W. P., Civetta, L., D'Antonio, M., Ferrara, G. & Necco, A. (2004). B/Nb and $\delta^{11}\text{B}$ systematics in the Phlegrean Volcanic District, Italy. *Journal of Volcanology and Geothermal Research* **133**, 123–139.
- Vetere, F., Botcharnikov, R. E., Holtz, F., Behrens, H. & De Rosa, R. (2011). Solubility of H₂O and CO₂ in shoshonitic melts at 1250°C and pressures from 50 to 400 MPa: Implications for Campi Flegrei magmatic systems. *Journal of Volcanology and Geothermal Research* **202**, 251–261.
- Villemant, B. (1988). Trace element evolution in the Phlegrean Fields (Central Italy): fractional crystallization and selective enrichment. *Contributions to Mineralogy and Petrology* **98**, 169–183.
- Vitale, S. & Isaia, R. (2014). Fractures and faults in volcanic rocks (Campi Flegrei, southern Italy): insight into volcano-tectonic processes. *International Journal of Earth Sciences* **103**, 801–819.
- Wallace, P. J. (2005). Volatiles in subduction zone magmas: concentrations and fluxes based on melt inclusion and volcanic gas data. *Journal of Volcanology and Geothermal Research* **140**, 217–240.
- Webster, J. D., Taylor, R. P. & Bean, C. (1993). Pre-eruptive melt composition and constraints on degassing of a water-rich pantellerite magma, Fantale volcano, Ethiopia. *Contributions to Mineralogy and Petrology* **114**, 53–62.
- Webster, J. D., Goldoff, B., Sintoni, M. F., Shimizu, N. & De Vivo, B. (2014). C–O–H–Cl–S–F volatile solubilities, partitioning, and mixing in phonolitic–trachytic melts and aqueous–carbonic vapor \pm saline liquid at 200 MPa. *Journal of Petrology* **55**, 2217–2248.
- Woo, J. Y. L. & Kilburn, C. R. J. (2010). Intrusion and deformation at Campi Flegrei, southern Italy: Sills, dikes, and regional extension. *Journal of Geophysical Research* **115**, B12210.
- Woods, S. C., Mackwell, S. & Dyar, D. (2000). Hydrogen in diopside: diffusion profiles. *American Mineralogist* **85**, 480–487.
- Zhang, Y. (1999). H₂O in rhyolitic glasses and melts: Measurement, speciation, solubility, and diffusion. *Reviews of Geophysics* **37**, 493–516.
- Zimmer, M. M., Plank, T., Hauri, E. H., Yogodzinski, G. M., Stelling, P., Larsen, J., Singer, B., Jicha, B., Mandeville, C. & Nye, C. J. (2010). The role of water in generating the calc-alkaline trend: new volatile data for Aleutian magmas and a new tholeiitic index. *Journal of Petrology* **51**, 2411–2444.
- Zollo, A., Maercklin, N., Vassallo, M., Dello Iacono, D., Virieux, J. & Gasparini, P. (2008). Seismic reflections reveal a massive melt layer feeding Campi Flegrei caldera. *Geophysical Research Letters* **35**, L12306.

